

Ph.D. Dissertation
University of Sopron (Soproni Egyetem)
Simonyi Károly Faculty of Engineering,
Wood Sciences and Applied Arts
The Cziráki József Doctoral School of Wood Sciences and Technologies

**Bacterial cellulose-Silk fibroin-Polyvinyl alcohol-
Silver nanocubes for flexible and transparent organic
light-emitting diode display**



Author: WORAKAN HOSAKUN
Research Supervisor: Prof. Dr. LEVENTE CSÓKA DSc.

Sopron
2018

Bacterial cellulose-Silk fibroin-Polyvinyl alcohol-Silver nanocubes for flexible and transparent organic light-emitting diode display

Értekezés doktori (PhD) fokozat elnyerése érdekében

a Soproni Egyetem Cziráki József Faanyagtudomány és Technológiák Doktori Iskolája Rosttechnikai és nanotechnológiai tudományok programja

Írta:
WORAKAN HOSAKUN

Készült a Soproni Egyetem Cziráki József Faanyagtudomány és Technológiák Doktori Iskola Rosttechnikai és nanotechnológiai tudományok programja keretében

Témavezető: Prof. Dr. Csóka Levente DSc.

Elfogadásra javaslom (igen / nem)

(aláírás)

A jelölt a doktori szigorlaton93..... % -ot ért el,

Sopron, 2018.06.07.

.....

elnöke

a Szigorlati Bizottság

Az értekezést bírálóként elfogadásra javaslom (igen / nem)

Első bíráló (Dr.) igen /nem

(aláírás)

Második bíráló (Dr.) igen /nem

(aláírás)

(Esetleg harmadik bíráló (Dr.) igen /nem

(aláírás)

A jelölt az értekezés nyilvános vitáján.....% - ot ért el

Sopron,

.....
a Bírálóbizottság elnöke

A doktori (PhD) oklevél minősítése.....

.....
Az EDHT elnöke

This is to certify that I, the undersigned *Worakan Hosakun*, hereby declare that this Ph.D. thesis entitled Bacterial cellulose-Silk fibroin-Polyvinyl alcohol-Silver nanocubes for flexible and transparent organic light-emitting diode display was carried out by me for the degree of Doctor of Philosophy in English under the guidance and supervision of Prof. Dr. Levente Csóka, Institute of Wood Based Products and Technologies, University of Sopron. This entire material belonging to my PhD dissertation, which now I submit for assessment, is entirely my own work except where due reference has been made in the text.

Sopron, December 7th, 2018

.....

Worakan Hosakun

Abstract

Transparent, light in weight, and flexible displays for organic light-emitting diode substrate (OLED) were studied. In this work, bacterial cellulose (BC), silk fibroin protein (SF), and/or polyvinyl alcohol (PVA) were chosen as raw materials. These materials are environmentally friendly and has biodegradability in order to decrease electronic wastes (e-waste). The BC-PVA, SF-PVA, pristine PVA, BC-SF, and BC-SF-PVA films obtained were further modified by impregnation with silver nanocubes (AgNC). Therefore, ten samples were achieved (S1 to S10), characterized by UV-vis, x-ray diffraction analysis (XRD), field emission scanning electron microscope (FESEM), attenuated total reflectance fourier transform infrared (ATR-FTIR) spectroscopy, differential scanning calorimetry (DSC), thermogravimetric analysis (TGA), tensile tester, dynamic mechanical analysis (DMA), and complex conductivity (conductance) and comparison of properties to the standard requirements of OLED display. The influences of the PVA and AgNC were also investigated. It was found that the transparency of the films significantly increased due to the presence of PVA polymer. In addition, PVA can better penetrate to the BC-SF fibrils than SF-PVA (S2) blended film because the inferior interaction between SF and PVA polymer occurs from PVA crystallization or the aggregation of SF molecular chains. AgNC was impregnated in the films and it was observed that PVA was a good dispersant confirmed by better uniform distribution and no aggregation of AgNC in PVA-AgNC film (S6), and BC-SF-PVA-AgNC film (S7) compared to SF-PVA-AgNC (S5) film. According to XRD results, it shows that the nanosilk was in amorphous state. In the case of ATR-FTIR analysis, the remarkable spectra was found at 3285 cm^{-1} that is corresponding to the BC stretching vibrations of inter-hydrogen bonding. This is owing to an improvement of the intermolecular H-bonds between OH groups of BC cellulose and NH in the amide groups of SF, in contrast with a decrease in intramolecular H-bonds of cellulose. However, AgNC did not affect the native structure of the films. In the case of DSC analysis, glass transition temperature (T_g) of all samples are showed the single temperature. The addition of BC (S1) increased the T_g of pure PVA, the hydrophilic character of both the BC and PVA, they are extremely miscible and thus the formation of strong hydrogen bond between the BC

and PVA matrix. Similar to S2, it presented high thermal stability which might be ascribed to the high crystallinity. Obviously, the glass transition peak of S7 was unrecognizable, only the endothermic peak appeared at 166.67°C due to the highly crosslinked structure of the substances. The thermal degradation behaviour from TGA and DTG curves showed that the samples which contained bacterial cellulose (S1, S4, and S7) initiate to degrade before 206°C for the main weight loss. The increasing in thermal stability was observed with the presence of the silver nanocubes in the BC, SF, and PVA films (S4, S5, S6, and S7). Dynamic mechanical analysis (DMA) indicated that the silver nanocubes affect the BC-SF and BC-SF-PVA films in a different way. This is probably a consequence of the reduced chain mobility of the SF chains induced by nanocubes. S7 film when studied the viscoelastic properties at elevated temperature showed very sensitive to the presence of light during the DMA experiment. The storage (E') and loss (E'') shear moduli curves of S7 film recorded in the dark and under illumination with white light are strongly related to the presence of silver nanocubes. The illumination probably induces similar effects in BC fibrils i.e. a rise in dipole moments, which are obviously amplified in the presence of silver nanocubes. These effects might not be significant below the glass transition temperature. However, above the glass transition, the mobility of the matrix chains is much higher and the photo-illumination effects may contribute to the shear forces induced by external periodic loading. For this reason, there is a strong influence of light on the position and intensity of the high-temperature relaxation transition in S7 sample. In the case of conductivity measurement, at the beginning of the test, the sample was kept in the dark and the white light was applied in the time interval from 47 to 67 s. It can be mentioned that PVA containing films are more sensitive to illumination. Obviously, photo-generation of the electrons does not depend solely of the presence of more conductive silver nanocubes. Flexible and transparent film for OLED display was successfully fabricated by using natural materials which are BC, SF and PVA modified with AgNC owing to high thermal stability, mechanical strength, and electrical conductivity.

Table of contents

Chapter	Page
Chapter I Introduction and Problem statement.....	15
1.1 Organic light-emitting diode (OLED) display.....	15
1.1.1 Working principle of OLED device.....	16
1.1.2 Types of OLED.....	17
1.2 Cellulose.....	20
1.2.1 Bacterial cellulose (BC).....	21
1.2.2 Bacterial cellulose production.....	23
1.3 Silk fibroin protein.....	25
1.3.1 Structure of silkworm cocoons.....	26
1.3.2 Silk fibroin Properties.....	28
1.4 Polyvinyl alcohol polymer (PVA).....	29
1.5 Cellulose and silk fibroin for flexible electronic substrate.....	31
1.6 Conductive materials for OLED device.....	31
1.7 Problem statement.....	34
Chapter II Materials and Methods.....	36
2.1 Raw materials and chemicals.....	36
2.2 Experimental details.....	36
2.2.1 Purification of Nata de coco and preparation of dried microfibrillated and nanocrystalline bacterial cellulose films.....	36
2.2.2 Degumming of silk cocoons and preparation of nano-silk fibroin films.....	37

2.2.3 Preparation of polyvinyl alcohol solution.....	38
2.2.4 Synthesis of silver nanocubes (AgNC).....	38
2.2.5 Fabrication of dried sample films by evaporation drying technique.....	39
2.3 Characterization methods used for testing the samples.....	40
2.3.1 Ultraviolet-visible (UV-VIS) spectroscopy.....	40
2.3.2 X-Ray Diffraction Analysis (XRD).....	41
2.3.3 Morphological analysis of the nanocomposite films by FE-SEM microscopy.....	41
2.3.4 ATR-FTIR spectroscopy.....	42
2.3.5 Differential Scanning Calorimetry (DSC).....	42
2.3.6 Thermogravimetric Analysis (TGA).....	43
2.3.7 Tensile tests of sample films.....	44
2.3.8 Dynamic mechanical analysis (DMA).....	44
2.3.9 Complex conductivity (Conductance).....	44
Chapter III Results and Discussions.....	46
3.1 The effect of acid hydrolysis on BC and SF fibres.....	46
3.2 Film characteristics.....	47
3.2.1 Optical transmittance.....	50
3.2.2 Transparent and flexible electronic display standard.....	51
3.3 Field Emission Scanning Electron Microscope analysis (FESEM).....	52
3.4 Angle Dispersive X-ray Diffraction (ADXRD).....	54
3.5 Attenuated total reflectance Fourier transform infrared spectroscopy.....	56

3.6 Differential Scanning Calorimetry (DSC).....	58
3.7 The thermogravimetric and derivative thermogravimetric analyses	60
3.8 Tensile strength.....	65
3.9 Dynamic mechanical analysis (DMA).....	66
3.10 Complex conductivity (Conductance).....	72
Chapter IV Conclusions.....	74
Chapter V References.....	80

List of Figures

Figure	Page
Figure 1.1 The evolution of television panels and constituting parts of LCD/LED vs OLED TV.....	16
Figure 1.2 A typical OLED parts and a basic small molecule organic light-emitting diode (SM-OLED) device structure.....	16
Figure 1.3 PMOLED structure.....	18
Figure 1.4 AMOLED structure.....	18
Figure 1.5 Transparent OLED structure.....	19
Figure 1.6 Top-emitting OLED structure.....	19
Figure 1.7 Hierarchical structures of wood.....	21
Figure 1.8 The model of BC microfibrils versus the fringed micelles of plant cellulose fibrils.....	22
Figure 1.9 Production of cellulose microfibrils by <i>Acetobacter xylinum</i>	25
Figure 1.10 Life cycle of silkworm	26
Figure 1.11 Constituent of raw silk, 2D schematic of the silk fibroin heavy chain and light chain, FTIR spectrum of silk fibroin thin film deposited on ITO/glass, and molecular structure of SF. The silk fibroin consists of turn (T), random coil (R), β - sheet, and side chain; according to the curve-fitting results.....	28
Figure 1.12 The structure of vinyl alcohol and PVA synthesized by the hydrolysis of polyvinyl acetate.....	30
Figure 1.13 DSC thermograms of neat PVA film.....	30
Figure 2.1 Raw Nata de coco and <i>Bombyx mori</i> silk cocoons.....	36
Figure 2.2 Purification of Nata de coco and purified BC.....	37

Figure 2.3 Hydrolyzed and degummed SF.....	38
Figure 2.4 Silver nanocubes synthesized by polyol process.....	39
Figure 2.5 Samples preparation, sputter coating, and FESEM instrument.....	42
Figure 2.6 DSC instrument and aluminum sample pans covered with the lids.....	43
Figure 2.7 TGA instrument and reference and sample pans were on a sensitive microbalance.....	44
Figure 2.8 Photo of the home-made cell used in photo-electrical characterizations of the films.....	45
Figure 3.1 Mechanism of acid hydrolysis of cellulose fibres.....	46
Figure 3.2 Optical images of transparent films of BC-PVA (S1), SF-PVA (S2), PVA (S3), BC-PVA-AgNC (S4), SF-PVA-AgNC (S5), PVA-AgNC (S6), BC-SF-PVA-AgNC (S7), BC-SF (S8), BC-SF-AgNC (S9), and BC-SF-PVA (S10) placed on a bookcover.....	48
Figure 3.3 Scattering regimes between wavelength (x-axis) vs particle size (y-axis).....	49
Figure 3.4 Transmittance versus wavelength graph for Polyethylene (PE), SF-PVA (S2), PVA (S3), SF-PVA-AgNC (S5), and PVA-AgNC (S6) substrates.....	50
Figure 3.5 FESEM images of BC-SF-PVA-AgNC (S7), SF-PVA (S2), and pure PVA film (S3).....	53
Figure 3.6 FESEM images of the distribution of silver nanocubes embedded in SF-PVA film (S5), the size of the isolated silver nanocubes, PVA-AgNC film (S6), and BC-SF-PVA-AgNC film (S7), the yellow points indicate the AgNC.....	54
Figure 3.7 Diffraction peaks of nanosilk.....	55
Figure 3.8 FT-IR spectra of BC-SF-PVA-AgNC (S7), BC-SF (S8), BC-SF-AgNC (S9), and BC-SF-PVA (S10) films.....	56

Figure 3.9 DSC second heating curves of BC-PVA (S1), SF-PVA (S2), pure PVA (S3), BC-PVA-AgNC (S4), SF-PVA-AgNC (S5), PVA-AgNC (S6), and BC-SF-PVA-AgNC (S7) at heating rate of 10 K/min.....	59
Figure 3.10 TGA and DTG curves of (S1) BC-PVA, (S2) SF-PVA, (S3) pure PVA, (S4) BC-PVA-Ag, (S5) SF-PVA-Ag, (S6) PVA-Ag, and (S7) BC-SF-PVA-Ag.....	61
Figure 3.11 Main chain of PVA reactions under heating.....	64
Figure 3.12 Stress vs Strain curves of BC-SF-PVA-AgNC (S7), BC-SF (S8), BC-SF-AgNC (S9), and BC-SF-PVA (S10) films.....	65
Figure 3.13 Storage and loss shear moduli of the films as a function of temperature. a) BC-SF (S8) and BC-SF-AgNC (S9) samples, b) BC-SF-PVA-AgNC (S7) and BC-SF-PVA (S10) samples. The measurements were carried out under the white light illumination.....	67
Figure 3.14 Storage and loss shear moduli of the BC-SF-PVA-AgNC (S7) film recorded in dark and under the white light illumination. The frequency of the external force was 1 Hz.....	68
Figure 3.15 Storage modulus (E') and dynamic loss tangent ($\tan \delta$) at different frequencies (a and b) of basic BC and BC-SF films.....	71
Figure 3.16 Specific conductance (G) and susceptance (B) of BC-SF-PVA-AgNC (S7), BC-SF (S8), BC-SF-AgNC (S9), and BC-SF-PVA (S10) films at 22 kHz as a function time. The samples were illuminated in the period from 47 to 67 s, which is indicated by vertical lines.....	72

List of Tables

Table	Page
Table 1.1 Level of Bacterial cellulose structure.....	23
Table 1.2 Mechanical properties of silkworm silk and other natural and synthetic fibrous materials.....	29
Table 1.3 The main criteria of a transparent electrode with expected performance for some applications. Plus signs indicate better values.....	32
Table 1.4 Regular information according to fabrication methods for transparent conductive material electrode.....	33
Table 2.1 Component of each sample.....	40
Table 2.2 Initial weight of DSC and TGA analysis.....	41
Table 2.3 The samples characterization.....	42
Table 3.1 Types and properties of flexible displays.....	51
Table 3.2 Spectral characteristics at various wavelengths for BC-SF-PVA-AgNC (S7), BC-SF (S8), BC-SF-AgNC (S9), and BC-SF-PVA (S10) films.....	57
Table 3.3 Differential Scanning Calorimetry Results of seven samples.....	59
Table 3.4 Degradation temperatures of S1, S2, S3, S4, S5, S6, and S7 determined by TGA and DTG results.....	62
Table 3.5 Mechanical strength of BC-SF, BC-SF-AgNC, BC-SF-PVA, and BC-SF-PVA-AgNC films.....	66
Table 3.6 Relative changes of specific conductance (ΔG) and susceptance (ΔB) of the films induced by illumination. Sample 7: BC-SF-PVA-AgNC, Sample 8: BC-SF, Sample 9: BC-SF-AgNC, Sample 10: BC-SF-PVA.....	73

List of Abbreviations

Ala	Alanine
AMOLED	Active-matrix organic light-emitting diode
ATR-FTIR	Attenuated total reflectance Fourier transform infrared
BC	Bacterial cellulose
BC-PVA	Bacterial cellulose embedded in polyvinyl alcohol
BC-PVA-AgNC	Bacterial cellulose embedded in polyvinyl alcohol and silver nanocubes
BC-SF	Bacterial cellulose embedded in silk fibroin
BC-SF-AgNC	Bacterial cellulose embedded in silk fibroin and silver nanocubes
BC-SF-PVA	Bacterial cellulose embedded in silk fibroin and polyvinyl alcohol
BC-SF-PVA-AgNC	Bacterial cellulose embedded in silk fibroin, polyvinyl alcohol and silver nanocubes
CTE	Coefficient of thermal expansion
DMA	Dynamic mechanical analysis
DSC	Differential Scanning Calorimetry
Gly	Glycine
FESEM	Field Emission Scanning Electron Microscope
FOLED	Foldable organic light-emitting diode
ITO	Indium tin oxide
OLED	Organic light-emitting diode

PMOLED	Passive-matrix organic light-emitting diode
PVA-AgNC	Polyvinyl alcohol embedded in silver nanocubes
Ser	Serine
SF-PVA	Silk fibroin embedded in polyvinyl alcohol
SF-PVA-AgNC	Silk fibroin embedded in polyvinyl alcohol and silver nanocubes
TGA	Thermogravimetric analysis
TOLED	Transparent organic light-emitting diode
XRD	X-ray Diffraction

CHAPTER I

INTRODUCTION AND PROBLEM STATEMENT

1.1 Organic light-emitting diode (OLED) display

In recent years, the development of flexible display has been taken place a flat panel for using in electronic devices, i.e. smartwatch, smartphone, and television panel. *Figure 1.1a* shows the evolution of television panels, development from cathode ray tube (CRT), plasma display panel (PDP), liquid crystal display (LCD), and liquid crystal display/light-emitting diode (LCD/LED), and organic light-emitting diode (OLED) TV screen. The distinction between LCD/LED and OLED can be described by *Figure 1.1b*. OLED is extremely thinner, with lighter, good viewing angle, and consumes less energy than LCD/LED. Therefore, one of the outstanding substrate is OLED which is the device made of organic semiconductor film. The backlight is not required and presents extremely thin screen, reduces the weight and greatly provides individual pixels that switch off for perfect black as the superior characteristics of OLED TV display. However, OLED technology is used mostly in phones nowadays. It is strongly becoming more prevalent, with over 400 million AMOLED screens manufactured in 2017 and continues growing in the market. Nowadays the smartphones are launching the new models to replace the obsolete devices every year, raise electronic wastes (e-waste) after a few short years of the consumers use. The out-of-date electronic wastes are rapidly filling the landfill sites of the globe. As such, the concerning for handling of e-waste issue is also an interesting topic. In this work, biodegradable materials were used for solving this e-waste problem. Generally, the producers use glass or plastic for fabricating display application. There are also polymer blends as one of the most capable methods to have new material with required properties. Therefore, bacterial cellulose (BC), silk fibroin protein (SF), and polyvinyl alcohol polymer (PVA) were studied in this work. First, each materials' characteristics and properties were explained. After that, the blended composites displays were reviewed.

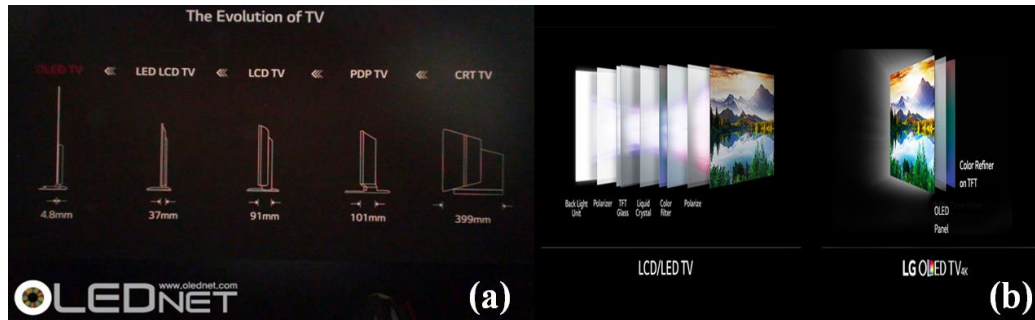


Figure 1.1 The evolution of television panels (a) and constituting parts of LCD/LED vs OLED TV (b). (“IFA 2015 Directions for LG Electronics’ OLED TV?”,2015; “What makes it the best TV ever”)

1.1.1 Working principle of OLED device

Six different layers of a simple OLED was depicted in *Figure 1.2a*. The top layer is sealed, the bottom layer is a substrate, followed by the anode (a positive terminal) and cathode (a negative terminal). The emissive layer, where the light is produced, and conductive layers are in between those layers.

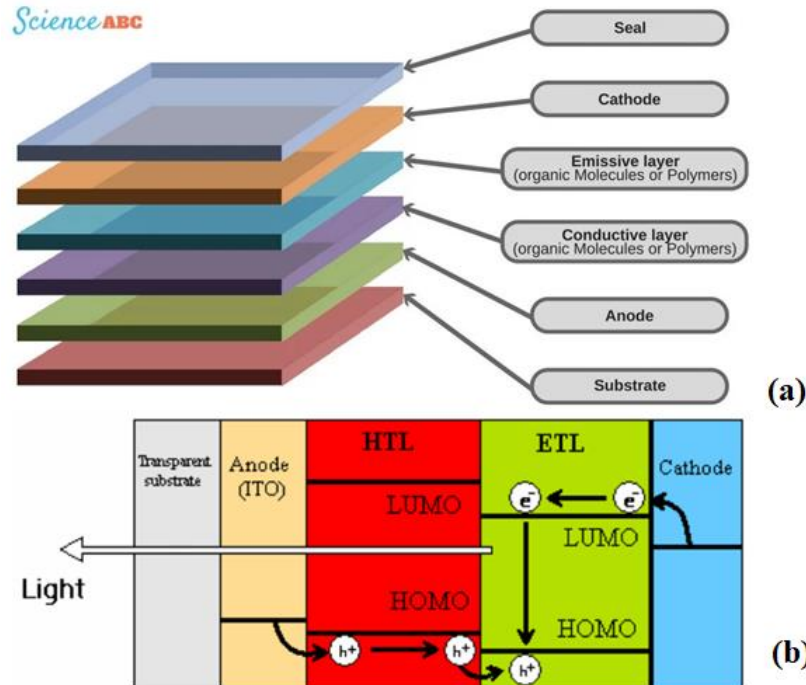


Figure 1.2 A typical OLED parts (a) and a basic small molecule organic light-emitting diode (SM-OLED) device structure (b). (“What is OLED and how does it work”, 2016; “OLEDs - Organic Light Emitting Diodes”, 2004)

Organic molecules were used to produce their electrons and holes. According to *Figure 1.2b*, when voltage is applied for making the OLED light up, the cathode starts receiving electrons and the anode begins losing them. The emissive layer changes to negatively charged and in contrast, the conductive layer becomes positively charged. The positive holes are more mobile than electrons, they cross the boundary from the conductive layer to the emissive layer. When a hole meets a negative electron, it occurred a rapid brief burst of energy in the form of photon. The OLED device produces continuous light in the process for as long as the power is on.

1.1.2 Types of OLED

Six types of OLED were distinguished: Passive and active matrix, transparent, top-emitting, foldable, and white OLED (Chen et al., 2003, Karzazi, 2014 and Kunić & Šego, 2012).

- *Passive-matrix OLED (PMOLED)*

The structure of PMOLED comprises of organic layers and strips of cathode positioned perpendicular to the anode strips (*Figure 1.3*). The layer where the pixels are generated is the intersection between anode and cathode. The brightness of each pixel depends on the proportional of the applied current amount. The turn on and off of the pixels rely on the applied external circuit to selected strips of anode and cathode. The advantages of PMOLED are easy and cheap to fabricate, and consume less power than an LCD and LED. On the other hand, PMOLED displays are usually small (up to 3 inches) and are used to display character data or small icons because of restriction in resolution and size: they are being used in MP3 players, mobile phone sub displays, etc. (Karzazi, 2014).

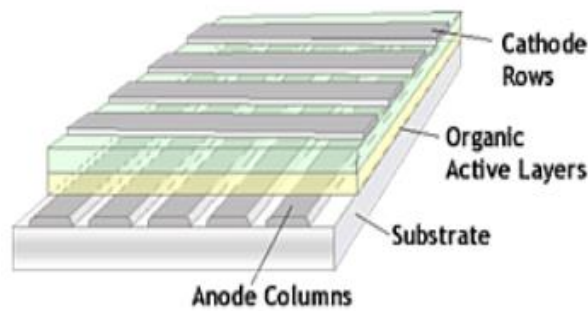


Figure 1.3 PMOLED structure (Kunić & Šego, 2012)

- Active-matrix OLED (AMOLED)

The AMOLED structure differs from PMOLED (*Figure 1.4*). It has full sheets of cathode, organic active layers and anode. In case of switching each pixel to turn on or off, a thin film transistor (TFT) plane in parallel to an anode is formed a matrix. Therefore, the display will show the black image whenever the pixels switch off which means that this can increase the battery life of the device. This OLED type is the least power consuming among others. The AMOLEDs are used for computer screens, large-screen TVs and electronic signs or billboards (Karzazi, 2014).

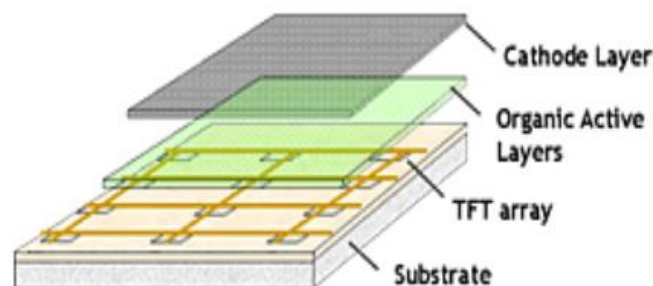


Figure 1.4 AMOLED structure (Kunić & Šego, 2012)

- Transparent OLED

The structure of transparent OLEDs (TOLEDs) has only transparent parts which are substrate, cathode and anode layers (*Figure 1.5*).

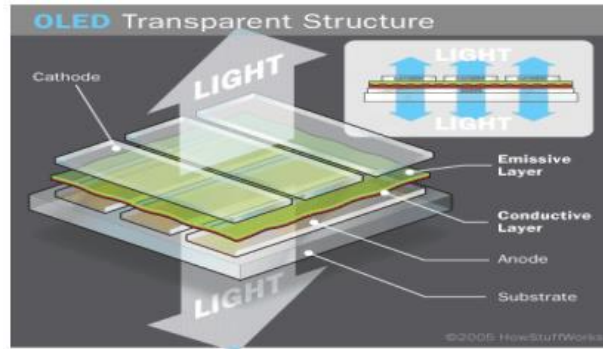


Figure 1.5 Transparent OLED structure (Kunić & Šego, 2012)

TOLED can be categorized into both the active and passive matrix OLED. According to all transparent components, light can pass to both directions when the display switches on. Thus, TOLED can produce screens that are top as well as bottom emitting. One advantage is it good contrast even in bright sunlight. The applications for TOLED are in head-up displays, laptops, mobile phones and smart windows (Karzazi, 2014).

- Top-emitting OLED

OLEDs that emit light from the top surface of devices refer to top-emitting OLED (Figure 1.6).

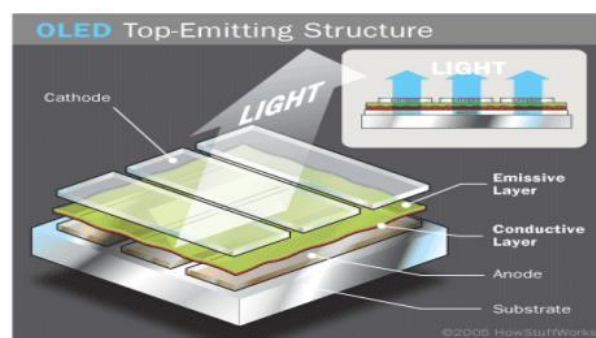


Figure 1.6 Top-emitting OLED structure (Kunić & Šego, 2012)

The substrate for top-emitting OLEDs can be both opaque and reflective e.g. a metal foil or silicon wafers. Top-emitting OLEDs are proper for pixel circuits in

active-matrix OLED since they can be more easily integrated with a non-transparent transistor backplane and can give higher display quality. Producers use this top-emitting OLED display in smart cards application (Karzazi, 2014 and Chen et al., 2003).

- *Foldable OLED*

Substrates for foldable OLEDs (FOLEDs) made of very flexible metallic foils or even plastics. The properties of FOLEDs are flexible, lightweight and durable. This type is mainly used in GPS devices, mobile phones, smart clothing, and large curved screen TVs. FOLEDs have rapid response time and high contrast images for television (Karzazi, 2014).

- *White OLED*

The last type of OLED is white OLEDs. This large sheet is cost-effective and also consumes less power than fluorescent lamps. The qualities of white OLEDs are creating the true-color of lighting and emit bright white light. It is used for car lighting because it can display very deep black as well as light and also very thin and lightweight (Karzazi, 2014).

1.2 Cellulose

The source of abundant and relatively cheap carbohydrate polymer – cellulose normally extracted from plants or their biomass. Cellulose is a polysaccharide derived from β -D-glucopyranose units comprising of a straight chain polymer where no branching presents with containing hundreds to above ten thousands linked D-glucose units by $\beta(1\rightarrow4)$ -glycosidic linkages and is an organic compound with a chemical formula of $(C_6H_{10}O_5)_n$. The microfibrils with high tensile strength were formed by the hydroxyl groups connected with oxygen atoms on the same chain or a neighbour chain of glucose, carrying the chains strongly together. Finally, cellulose microfibrils are meshed and become a cell wall as depicted in *Figure 1.7*, generating the high tensile

strength. Cellulose has several crystalline structures based on the location of hydrogen bonds, resulted in a complicated organization (cellulose I, II, III, and IV structures). Cellulose I is the natural or native cellulose. It comprises of rod-like crystalline microfibrils with the different structure I_α and I_β . Bacteria and algae can produce cellulose I_α while I_β was mainly found in cellulose in high plants. Cellulose II comes from regenerated cellulose fibres which is more stable allomorph. With different kinds of chemical treatments, cellulose III and cellulose IV were produced from cellulose I. The properties of cellulose are odorless, hydrophilic, insoluble in water and most organic solvents, and biodegradable (Li, Y, 2014). According to these great characteristics, demand on derivatives of plant cellulose is increasing and had increased wood consumption as raw material. It caused deforestation and global environmental problem.

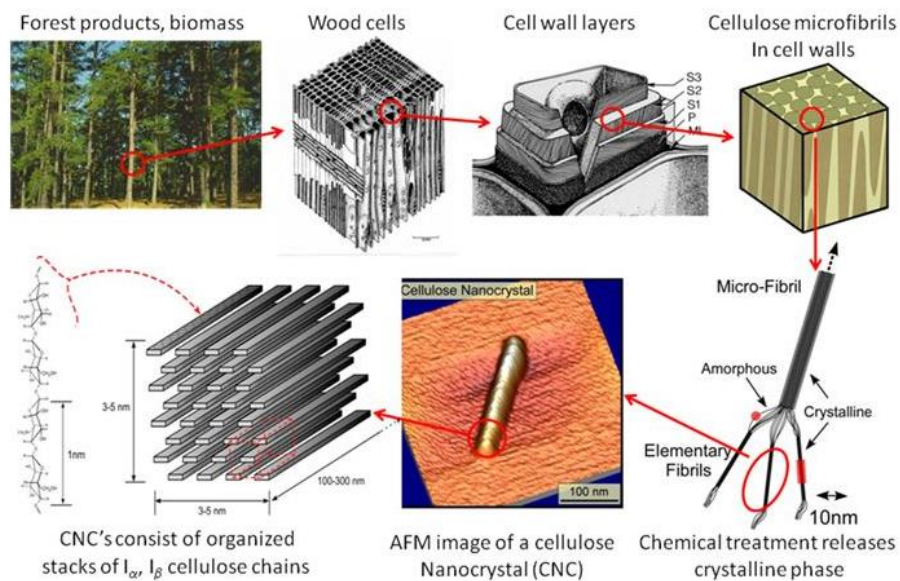


Figure 1.7 Hierarchical structures of wood (“Size Scale of Cellulose-based Particles”)

1.2.1 Bacterial cellulose (BC)

In spite of the fact that plant is the major contributor of cellulose, many bacteria are also able to produce cellulose. Bacterial cellulose is an extracellular product made by some bacteria belonging to the genera *Acetobacter*, *Rhizobium*, *Agrobacterium*, *Aerobacter*, *Achromobacter*, *Azotobacter*, *Salmonella*, *Escherichia*, and *Sarcina* were

first reported by Brown in 1988 (Sulaeva, Henniges, Rosenau, & Potthast, 2015). It was first served as a diet food in Asia and also as a traditional dessert in Philippines called nata de coco (Foresti, Vázquez, & Boury, 2017). Many researches on BC indicated that it is chemically similar to plant cellulose, but its macromolecular structure and properties are unlike the latter, exhibited in *Figure 1.8*. Subfibrils were formed by aggregation of nascent chains of BC. Then, they were crystallized into microfibrils, these into bundles, and finally the latter into ribbons (“Bacterial cellulose”). As shown in *Table 1.1*, the structure levels of BC are also presented. The BC structure has abundant surface of hydroxyl groups that describing it as hydrophilic, biodegradable, and chemical-modifying capacity. According to its unique properties, BC has gained much attention in the field of material science and biomedical applications such as wound dressing and blood vessel regeneration (Foresti, Vázquez, & Boury, 2017).

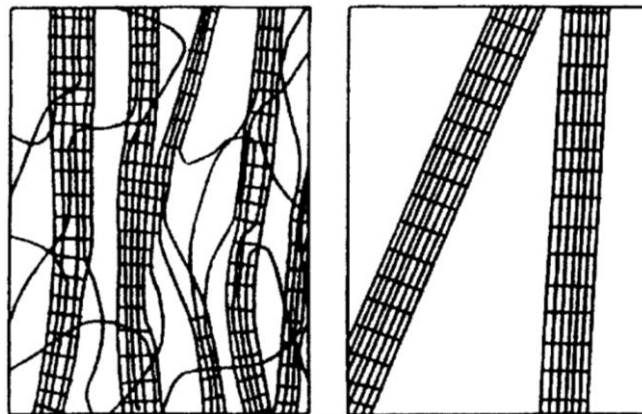
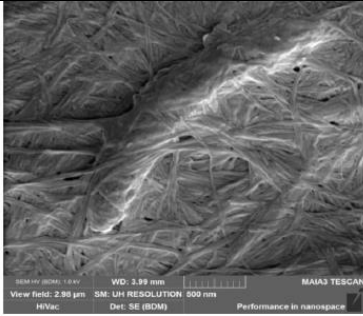
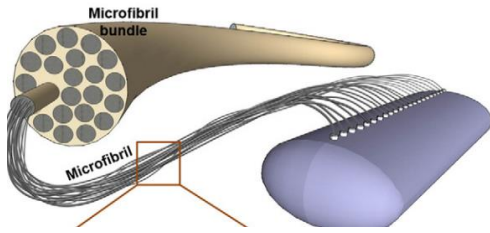
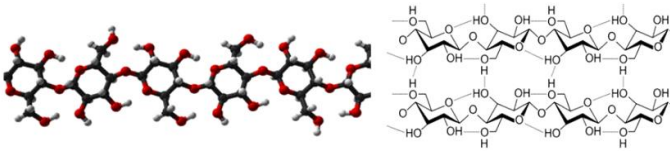
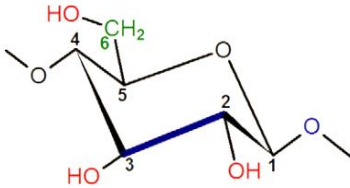


Figure 1.8 The model of BC microfibrils (right) versus the fringed micelles of plant cellulose fibrils (left) (“Bacterial cellulose”)

Table 1.1 Level of Bacterial cellulose structure

	Overview of BC structural organization	References
3-dimensional network structure		(Y Hosakun, Halász, Horváth, Csóka, & Djoković, 2017)
Microfibril bundle to microfibrils		(Sulaeva, Henniges, Rosenau, & Potthast, 2015)
Polymer chain		(Foresti, Vázquez, & Boury, 2017)
Monomer unit		(Sulaeva, Henniges, Rosenau, & Potthast, 2015)

1.2.2 Bacterial cellulose production

In this work, bacterial cellulose from *Acetobacter* species was used. This cellulose production was initially discovered by A.J. Brown in 1886. He investigated that in the presence of oxygen and glucose, the resting cells of *Acetobacter* were produced cellulose (Chawla, Bajaj, Survase, & S. Singhal, 2009).

Bacterial cellulose which can be produced in different forms is fermented under static, agitated, or even stirred conditions. The static condition produces three-dimensional interconnected reticular pellicle. On the other hand, irregular shape sphere-like cellulose particle is formed by agitating and stirring conditions. The production of cellulose under static condition has to supply by air from medium surface and the concentration of the carbon source effect the yield also. However, the

formation of BC with hydrogen and C-H bonding will increase by the increasing of growth time. Bacteria turn into inactive because of insufficient oxygen source. The pellicles will growth downward when the process reaches its limit and all bacteria are entrapped. In order to producing cellulose from bacteria (*Figure 1.9*), possibility of operation present in the pentose-phosphate cycle or the Krebs cycle, relying on the physiological state of the cell coupled with gluconeogenesis (K.-Y. Lee, Buldum, Mantalaris, & Bismarck, 2014). The oxidation of carbohydrates referred to the pentose-phosphate cycle, on the other hand, the Krebs cycle associates with the oxidation of acetate-derived carbohydrates, fat, and proteins. Individual enzymes, catalytic complexes, and regulatory proteins are all involved in the biosynthesis of cellulose which contains four key enzymatic steps when carbon source is glucose. Phosphorylation of glucose by glucokinase comes first, followed by isomerization of glucose-6-phosphate (Glc-6-P) to glucose-1-phosphate (Glc-1-P) by phosphoglucomutase, after that synthesis of UDPglucose (UDPGlc), which is common in many organisms and the direct cellulose precursor, by UDPG-pyrophosphorylase (UGPase), and finally, cellulose synthase reaction. Two processes of synthesized cellulose are in microorganisms. 1,4- β -glucan chains formation and the assembly and crystallization of cellulose chains. The cellulose molecules are started to synthesize inside the bacteria. Then, these molecules are formed protofibrils by spun through cellulose export components. These protofibrils are then formed a ribbon shaped microfibril. The glucose unit is catalyzed by cellulose synthase and become into the 1,4- β -glucan chains (K.-Y. Lee, Buldum, Mantalaris, & Bismarck, 2014).

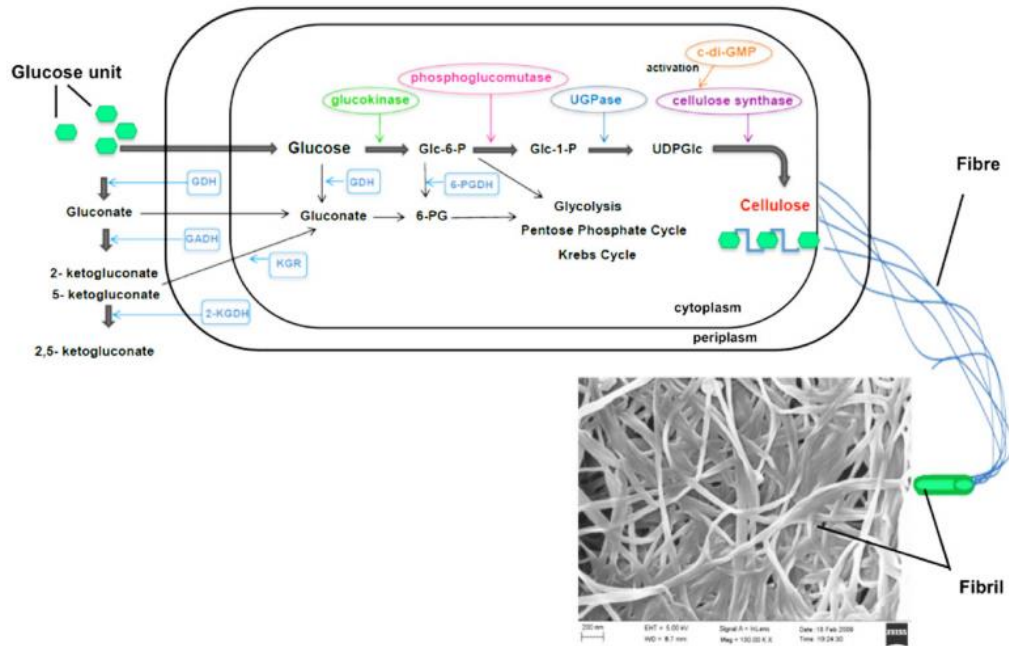


Figure 1.9 Production of cellulose microfibrils by *Acetobacter xylinum* (K.-Y. Lee, Buldum, Mantalaris, & Bismarck, 2014)

The alkaline treatment of BC pellicles for purification of BC fibrils has been described (Tsalagkas, 2015 and Santos et al., 2015). Most of non-cellulosic materials, proteins and nucleic acids, and other impurities were eradicated by cell lysis (breaking down of the cell) and chemical bond breakage from alkali treatment to achieve pure BC. Sodium hydroxide (NaOH) in large amounts can solubilize amorphous cellulose which enhances the material crystallinity, purity, and viscosity. Therefore, the crystalline cellulose was formed (Santos et al., 2015). Generally, the common procedure of this treatment use 0.1 M NaOH solution with warm conditions because alkali can well penetrate into the fibrils than at the ambient conditions (Tsalagkas, 2015).

1.3 Silk fibroin protein

Silk fibroin (SF) is a fibroin protein-based polymer which is produced by spiders, silkworms, scorpions, mites, and flies (Melke, Midha, Ghosh, Ito, & Hofmann, 2016 and Shang, Zhu, & Fan, 2013). Normally, *Bombyx mori* silk cocoons are mainly consisted of 72–81% of a fibrous protein fibroin core and a surrounding

19–28% sericin protein. Silk fibroin protein has discovered for various applications such as tissue engineering or other biomedical applications because of its high tensile strength, biocompatibility, biodegradability, and non-cytotoxicity (Acharya, Ghosh, & Kundu, 2008). In this work, *Bombyx mori* silkworm cocoons were used. Generally, the total life-cycle of silkworm ranges from 6-8 weeks. As shown in this *Figure 1.10*, in brief, tiny eggs hatch out into a tiny black caterpillar. Then, it eats mulberry leaves and goes through four molts. The caterpillar spins a cocoon of silk threads around itself. Starting the pupa state, the caterpillar changes itself inside the cocoon. The silk threads from the cocoon are used in manufacture to produce many products. Hundreds of milligrams of silk proteins were produced from one larva to make a robust cocoon (Teramoto & Kojima, 2014).



Figure 1.10 Life cycle of silkworm (“Silk”, 2016)

1.3.1 Structure of silkworm cocoons

The raw silk comprises of silk fibroin protein covered with sericin protein on their surfaces as presented in the *Figure 1.11a* (Koh et al., 2015). Sericin protein consist of different polypeptides (weight of 24 to 400 kDa), on the surface of cocoon. They are identified by eccentric 40% of serine content together with 16% of glycine

(Kundu, Dash, Dash, & Kaplan, 2008). Normally, sericin has five types of polypeptides, s-1, s-2, s-3, s-4, and s-5. They have been reported from different parts of the middle silk gland (MSG) and s-1, s-2, and s-3 are the main components. Serine, glycine, and aspartic acid were observed in the polypeptides. Some researchers reviewed the applications of sericin as skin care for anti-wrinkle, anti-aging effect, moisturizing, conditioning, and cleansing properties etc. (Kundu, Dash, Dash, & Kaplan, 2008 and J. H. Lee, Song, Park, & Um, 2016). In case of amino acid constituent of silk fibroin primarily consists of glycine (G), alanine (A), and serine (S) in the molar ratio of 3:2:1. *Figure 1.11b* displays silk fibroin basic structure. Silk fibroin composes of a light chain (~25 kDa) and a heavy chain (~390 kDa) in the ratio 1:1 connected by a single disulphide bond. The alignment of silk fibroin along the fiber axis linked together by the network of hydrogen bonds interchain could form β -sheet structures. In *Figure 1.11c*, Hota et al., 2012 studied to produce the biomaterial for bio-memristor devices from silk fibroin protein. From the infrared absorption spectra of static amide I region, they found that the observed spectrum comes from the secondary structure of SF. Fourier deconvolution method was considered to obtain more information. β -sheets structures (B), turn structures (T), alpha-helix (A), random coil (R), and side chains (SC) were found. It can be concluded that SF film presented amorphous structure.

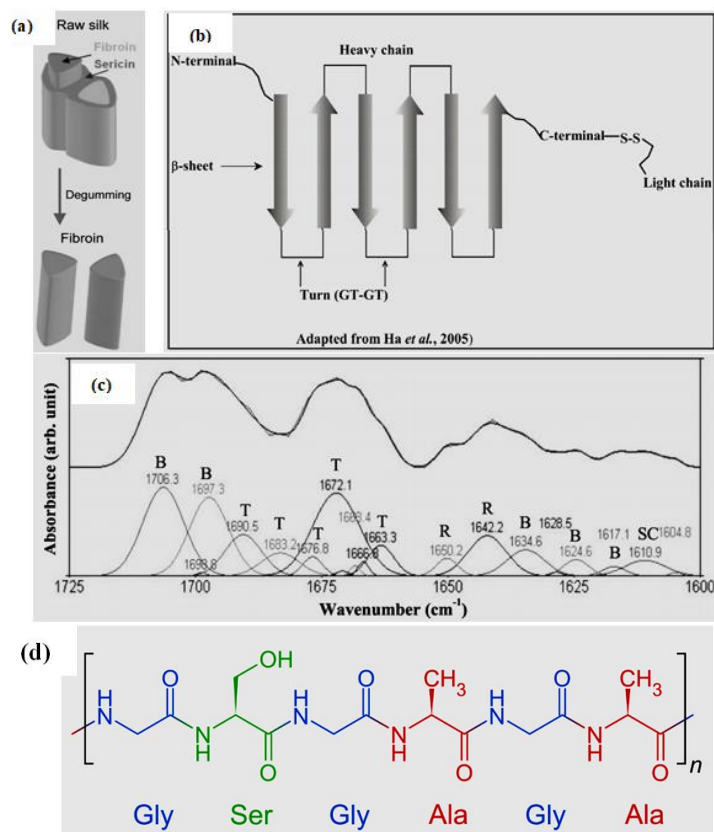


Figure 1.11 Constituent of raw silk (a), 2D schematic of the silk fibroin heavy chain and light chain (b), FTIR spectrum of silk fibroin thin film deposited on ITO/glass (c), and molecular structure of SF (d). The silk fibroin consists of turn (T), random coil (R), β -sheet, and side chain; according to the curve-fitting results (Hota, Bera, Kundu, Kundu, & Maiti, 2012, Ha, Gracz, Tonelli, & Hudson, 2005, and “Unit - Chemistry of Garments: Animal Fibres”, 2016)

In order to separate fibroin from sericin (silk gum), a conventional process known as degumming is considered. Raw silkworm cocoons were degummed by thermo-chemical treatment, resulting in the changes in microstructure of fibroin and mechanical properties (Jiang et al., 2006). In general raw silk may be degummed by submerging the cocoon in boiling water, sometimes with detergent or salt to improve the treatment efficiency. The sericin which is eliminated will be in the liquor’s suspension.

1.3.2 Silk fibroin Properties

According to *Table 1.2*, the mechanical properties of silkworm and some other fibrous material were presented. Both breaking strain and toughness of silk fibroin fibre has higher values than Kevlar. Besides, Wu et al., 2009 claimed that the mechanical properties of silk are closely correlated with its hierarchical structures.

Table 1.2 Mechanical properties of silkworm silk and other natural and synthetic fibrous materials (Koh et al., 2015)

Materials	Young's modulus (GPa)	Ultimate strength (MPa)	Breaking strain (%)	Toughness (MJ m⁻³)
Silkworm silk fibroin <i>(Bombyx mori)</i>	10-17	300-740	4-26	70-78
β-sheet crystallites <i>(Bombyx mori)</i>	16-18	n/a	n/a	n/a
Spider silk (<i>Nephila clavipes</i>)	10.9	875	16.7	n/a
Nylon	1.8-5	430-950	18	80
Kevlar	130	3600	2.7	50
Wool	0.5	200	50	60

1.4 Polyvinyl alcohol polymer (PVA)

Polyvinyl alcohol (PVA), a synthetic polymer, is a partial or full hydrolysis product of polyvinyl acetate for eliminating the acetate groups and a water-soluble polymer as shown in *Figure 1.12* and has high tensile properties (24 to 79 MPa) (Bondeson & Oksman, 2007). PVA has the advantages of good film forming properties and high resistance to water, oil, grease, and solvent makes it adaptable for various applications (Baker, Walsh, Schwartz, & Boyan, 2012). It is known as a biodegradable material, biocompatible, nontoxic, noncarcinogenic and extensively used in paper sizing, fiber coating, adhesives, emulsion polymerization, and medical field (Kawai & Hu, 2009). Also, PVA films present outstanding barrier properties for food packaging systems.

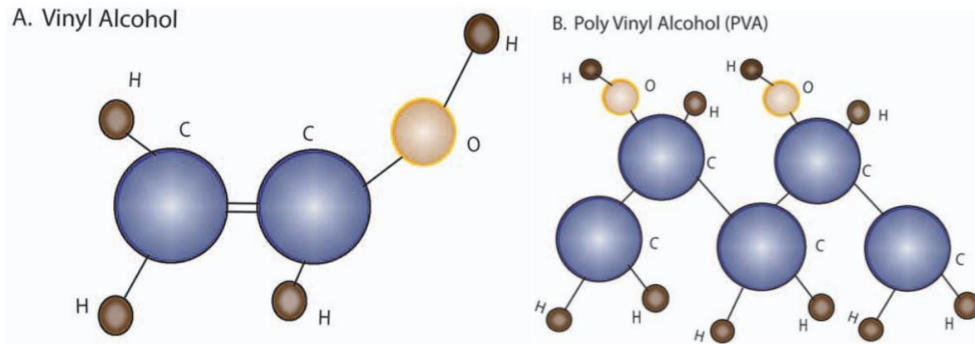


Figure 1.12 The structure of vinyl alcohol (left) and PVA synthesized by the hydrolysis of polyvinyl acetate (right) (Baker, Walsh, Schwartz, & Boyan, 2012)

According to *Figure 1.13*, an endothermic curve at 221°C was presented. T_g of PVA was noted at 70°C. However, many researches were attempted to blend PVA with other material to form thin-films or membranes. Lu et al., 2008 also revealed that cellulose and PVA polymer matrix has a good dispersion caused a good reinforcement. The interpenetration of PVA molecules into cellulose structure comes from the long duration of mixing. The hydroxyl groups on PVA interact with the hydrophilic surfaces of the cellulose. The high transparency film was presented as a result of the homogeneous dispersion of cellulose in PVA. They found that after cellulose presence, the crystallinity of PVA was increased owing to the nucleating effect of nano-sized cellulose fibers.

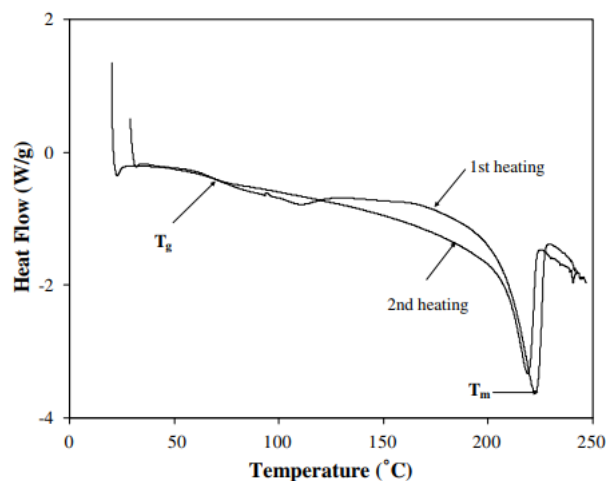


Figure 1.13 DSC thermograms of neat PVA film (Lu, Wang, & Drzal, 2008)

1.5 Cellulose and silk fibroin for flexible electronic substrate

Okahisa et al., 2009 studied the cellulose nanofibres from Douglas fir (*Pseudotsuga menziesii*) reinforced with acrylic matrix resins to fabricate a substrate for flexible organic light-emitting diode displays. They mentioned that the thickness of nanocomposite films were 90-100 μm and presented the light transmittance in the range of 82-85%. Moreover, these nanocomposites possess appropriate mechanical properties for continuous roll-to-roll processing. Legnani et al., 2008 used BC as flexible substrates for fabricating the organic light emitting diodes (OLED). Indium tin oxide (ITO) as a transparent conductive layer was functionalized on BC membrane. Normally, ITO was used for optoelectronic applications owing to its high transmittance in the visible region and high conductivity. SiO_2 was also deposited by magnetron sputtering for increasing the smoothness of the film surface and to avoid surface reactions between the BC substrate and the deposited ITO film. They found that it produced highly effective in light emission and performance of the OLED device. Ummartyotin et al., 2012 also studied the development of a transparent and flexible BC and poly-urethane (PU) based resin nanocomposite film as a substrate for OLED display. They suggested that the characteristics of flexibility, optical transparency, high of light transmittance and dimensional stability in terms of coefficient of thermal expansion (CTE) of as low as 18 ppm/K was achieved the criteria for OLED substrate. Liu et al., 2014 used natural SF films as substrates instead of glass or synthetic polymers and blended it with silver nanowires (conductive material). The substrate presented a conductivity about 11 Ω/sq together with a transparency of more than 80% at 600 nm. According to the measurement of resistance after bending test, the resistance of the substrates slightly raises after being bent 500 times, but maintained lower than 20 Ω/sq . That is better than traditional flexible indium stannum oxide-polyethylene naphthalate (ITO-PEN) substrates.

1.6 Conductive materials for OLED device

Table 1.3 exhibited general information about the average requirements of some type applications. Indium tin oxide (Indium stannum oxide) (ITO) has been the most widely used anode material in OLED and LCD. The important properties are

high transparency ($\sim 90\%$ at 550 nm), low resistivity ($\sim 2 \times 10^{-4} \Omega \text{ cm}$), and relatively high work function ($\sim 4.8 \text{ eV}$) but its elements are becoming increasingly expensive, and it is brittle, causing it unreasonable for flexible screen. Therefore, it is desirable to develop other possibilities for transparent and flexible electrodes.

Table 1.3 The main criteria of a transparent electrode with expected performance for some applications. Plus signs indicate better values from very good (+++) to acceptable (+) (Daniel et al., 2013)

Application	Transparency	Conductivity	Flexibility
Photovoltaics	+++	+++	+
OLED/PLED	++	++	+
Film heaters	+	+++	++
Touch screens	+++	++	++

Graphene is a good candidate for conductive materials but it has disadvantage that it shows poorer current efficiencies than ITO-based devices (T.-H. Han et al., 2012). One of the favourable materials is silver, it has remarkable characteristics. It can produce the highest electrical conductivity, transparent conductive electrodes for optoelectronics, and the lowest optical losses of all metals (Berkhout, 2015). In this manner, AgNWs was used and can be covered onto flexible substrates by cost-effective and scalable roll-to-roll fabrication. According to *Table 1.4*, it represents the needs of each electrode for fabrication. The ranges of temperature were corresponding to the processing temperature during device fabrication.

Table 1.4 Regular information according to fabrication methods for transparent conductive material electrode. Plus signs indicate very good (+++), good (++), and acceptable (+) (Daniel et al., 2013)

Fabrication method	Transparent conductive oxides (TCOs)	Graphene	Carbon nanotube networks (CNTs)	Silver nanowires (AgNWs)
Chemical vapour deposition	+++	+++	+	-
Sputtering	+++	-	-	-
Spin coating	-	+	++	++
Spray deposition	++	+	+++	+++
Screen printing	--	+	++	++
Cost	Low-High	High	High	Medium
Processing temperature (°C)	>200 ^b -1000	RT-1000 ^c	RT-700 ^c	RT-700 ^c
Uniformity	+++	+ to +++	++	++
Typical thickness (nm)	100-300	<5	<10	25 > 600 ^d
Typical transmission (at 550 nm)	80-97%	80-96%	80-91%	80-96%

^aFabrication method refers to the production of electrodes directly, not to the production of the constituent components which are used to fabricate the network.

^bDeposition temperatures of TCOs usually require several hundred degrees celsius or the use of vacuum processes such as sputtering.

^cNetworks can be fabricated at room temperature (RT) but if device fabrication requires high temperature processes vacuum or encapsulation are required to stabilize the films.

^dThickness is diameter and density dependent though with high mechanical pressure it can be reduced to the diameter of a single nanowire.

1.7 Problem Statement

Regarding to the frequent changing of the new trend of smartphone nowadays, many people simply decide to replace it with the latest flagship after having it for 2 or 3 years, hence, the problems of electronic wastes are going to increase. The main objective of this work was to prepare and investigate the properties of the flexible, thin, and transparent composite films produced from bacterial cellulose (BC), silk fibroin protein (SF), polyvinyl alcohol polymer (PVA), silver nanocubes (AgNC) making a substrate for organic light-emitting diode (OLED). These materials are environmentally friendly. This implies that they are biodegradable and are easily decompose. The minor objectives are defined to reach the goals as follow;

Objective I: Preparation of flexible and transparent substrate for OLED display

Bacterial cellulose, silk fibroin protein, polyvinyl alcohol, silver nanocubes were used to prepare the thin films for OLED substrate. To the best of our knowledge, this is the first invention of the flexible displays by using these materials mixed together. BC and SF fibrils were first hydrolyzed by fuming acid to obtain the nano-size fibrils. Then, ten samples were prepared; BC-PVA (S1), SF-PVA (S2), PVA (S3), BC-PVA-AgNC (S4), SF-PVA-AgNC (S5), PVA-AgNC (S6), BC-SF-PVA-AgNC (S7), BC-SF (S8), BC-SF-AgNC (S9), BC-SF-PVA (S10). In case of AgNC, it was synthesized and used as a conductive material.

Objective II: Investigation of physical, mechanical, thermal, and electrical properties of ten samples

First, the visually transparent of each film were compared by photographs. Then, the properties of ten films were studied by using UV-Vis spectroscopy, XRD, FESEM, ATR-FTIR, DSC, TGA, Tensile tester, DMA, and Complex conductivity analysis. The effect of PVA, AgNC, and acid hydrolysis were also examined. Some of those films were performed on the influence of light and investigate the mechanical and conductivity properties.

Objective III: Comparison the characteristics of these samples according to the Standard requirement of flexible electronic display

Not only the basic properties need to studies, but the requirements of these substrates also important to consider. Recently, the flexible electronic substrate has the standard regulations. Therefore, our films need to be compared with glass, plastic, or other polymer composite films. Finally, our ten substrates were chosen for the preferential to further fabricate the OLED display for smartphone.

CHAPTER II

MATERIALS AND METHODS

2.1 Raw materials and chemicals

Nata de coco was kindly supplied by Thongaumphai's production, Thailand. Cocoons of silkworm *Bombyx Mori* were obtained from Chul Thai Silk Co., Ltd., Thailand. Sodium hydroxide (NaOH), sodium carbonate (Na₂CO₃), 37% hydrochloric acid solution (fuming HCl), polyvinylpyrrolidone (PVP), polyvinyl alcohol (PVA), potassium bromide (KBr), ethylene glycol (EG), copper(II) chloride (CuCl₂), silver nitrate (AgNO₃), and methanol (CH₃OH) were purchased from Sigma-Aldrich Co., Hungary. All chemicals were used as received without further purification (Figure 2.1).



Figure 2.1 Raw *Nata de coco* (left) and *Bombyx mori* silk cocoons (right)

2.2 Experimental details

2.2.1 Purification of *Nata de coco* and preparation of dried microfibrillated and nanocrystalline bacterial cellulose films

The procedure for the purification of *Nata de coco* and preparation of dried BC films are based on Y Hosakun et al., 2017, briefly, raw *Nata de coco* was first cut and boiled in water until reached pH~7. Then, it was purified in 0.1 M NaOH solution at 80°C to eliminate non-cellulosic materials. This process changed the color from yellow to transparent gel. Then, the gel was boiled in distilled water several times until the pH become neutral. The gel was blended by a blender and dried in an oven to

get dried microfibrillated BC films (*Figure 2.2*). These films were further used for preparing nanocrystalline BC films.



Figure 2.2 Purification of Nata de coco (left) and purified BC (right)

The dried microfibrillated BC films (approximately 1.2 g) were placed in a desiccator which contained 37% HCl solution inside. The degradation of cellulose occurred and the nanocrystalline cellulose was achieved during this step. Then, it was dried in an oven to calculate the remaining weight of BC after hydrolysis (~ 1.1 g was prepared for further analyses).

2.2.2 Degumming of silk cocoons and preparation of nano-silk fibroin films

The process of degumming of silk cocoons was carried out similar to Y Hosakun, Halász, Horváth, Csóka, & Djoković, 2017, briefly, the cocoons were boiled in 0.02 M Na_2CO_3 and washed in water for several times at 50°C. Then, the degummed SF was put into an oven to dry. According to hydrolysis reaction, the dried degummed SF (approximately 0.7 g) was placed into desiccator with 37% HCl vapor inside to obtain nano-silk fibroin (*Figure 2.3*). The nanosilk was then dried in an oven for calculating the weight after hydrolysis (~ 0.5 g was prepared for further analyses).



Figure 2.3 Hydrolyzed and degummed SF

2.2.3 Preparation of polyvinyl alcohol solution

In order to prepare 5%wt PVA solution, 2.5 g PVA powder was dissolved in 50 ml distilled water. After that, the solution was heated and continuously stirred at 95°C for 2 hours until clear solution obtained. Approximately 50 mL of solution was prepared for further use.

2.2.4 Synthesis of silver nanocubes (AgNC)

In order to synthesize AgNC, a mixture of 0.668 g of PVP, 0.010 g of KBr, and 20 ml of EG was heated and kept temperature constant in a flask at 170°C with continuous stirring. Subsequently, 0.050 g CuCl_2 was added to the flask. The combined solution was allowed to mix for 3 minutes. Then, 0.220 g of AgNO_3 powder was titrated for 10 minutes into the flask. To ensure the growth to be completed, the flask was heated for 2 hours. After the solution was cooled down, it was centrifuged at 2000 rpm for 30 minutes to separate the cubes which remained in the supernatant. The supernatant was then centrifuged twice to precipitate the cubes at 6000 rpm for 30 minutes. After the supernatant which contain EG, PVP, and other impurities was discarded, the sediment of AgNC was stored in 5 ml of methanol (Hu, Kim, Lee, Peumans, & Cui, 2010) (*Figure 2.4*).



Figure 2.4 Silver nanocubes (AgNC) synthesized by polyol process

2.2.5 Fabrication of dried sample films by evaporation drying technique

- S1 was prepared by blending of micro- and nanofibrillated BC at an amount according to *Table 2.1*. Both types of BC were soaked in 80 mL of distilled water and the obtained dispersed colloid was treated in an ultrasonic instrument at low frequency (20 kHz) using a horn with a tip diameter of 18 mm. The suspension of BC after sonication was mixed with PVA solution and stirred overnight.
- S2 was fabricated from nanosilk and PVA. First, SF was immersed in water of 80 mL. After that, it was sonicated until well dispersed colloid was achieved. PVA solution was blended to the suspension and stirred overnight.
- S3 contained only PVA solution.
- S4 was prepared similar to S1 but AgNC was added into the colloid.
- S5 was made according to S2 except blending of AgNC.
- S6 was similar to S3 and embedded with AgNC.
- S7 was blended for all components. Firstly, both types of BC and nanosilk were immersed in 80 mL of distilled water and to achieve dispersed colloid, an ultrasonic instrument at low frequency (20 kHz) was applied. The suspension after sonication was mixed with PVA and AgNC solution, then, stirred overnight.
- S8 comprised of BC and SF. Micro- and nanofibrillated BC and nanosilk were steeped in 80 mL of distilled water and an ultrasonic instrument was applied to obtain well dispersed colloid.
- S9 was prepared similar to S8 and blended with AgNC.
- S10 was fabricated by mixing of BC, SF, and PVA analogous to S9, no AgNC.

The samples were poured onto trays (diameter 7 cm). The trays were put in an oven at 40°C for 3 days until the dried films were obtained. Ten types of the flexible and transparent samples were obtained according to *Table 2.1* below.

Table 2.1 Component of each sample

Sample code	Microfibrillated BC dried film (mg)	Nanofibrillated BC dried film (mg)	Dried Nanosilk (mg)	5% wt PVA solution (mL)	AgNC (mL)
S1	20	60	-	1	-
S2	-	-	26.7	1	-
S3	-	-	-	1	-
S4	20	60	-	1	0.07
S5	-	-	26.7	1	0.07
S6	-	-	-	1	0.07
S7	20	60	26.7	1	0.07
S8	20	60	26.7	-	-
S9	20	60	26.7	-	0.07
S10	20	60	26.7	1	-

Three pieces of each samples (S1-S10) were prepared for further analysis.

2.3 Characterization methods used for testing the samples

The ten different types of samples were characterized by using eight types of measurements discussed below. Not all samples were used in every test (*Table 2.2*).

2.3.1 Ultraviolet-visible (UV-VIS) spectroscopy

Ultraviolet-visible (UV-Vis) spectra were investigated on WPA lightwave S2000 UV/VIS spectrophotometer for recording the light transmittance of the samples over the visible wavelength of 400-800 nm. A base line was recorded and calibrated using air. Measurement was conducted in triplicates.

Table 2.2 The samples characterization. Performed (✓) and not performed (-)

Sample Code	Light transmittance	FESEM	FTIR	DSC	TGA	Tensile strength	DMA	Conductance
S1	✓	✓	-	✓	✓	✓	-	-
S2	✓	✓	-	✓	✓	✓	-	-
S3	✓	✓	-	✓	✓	✓	-	-
S4	✓	✓	-	✓	✓	✓	-	-
S5	✓	✓	-	✓	✓	✓	-	-
S6	✓	✓	-	✓	✓	✓	-	-
S7	✓	✓	✓	✓	✓	✓	✓	✓
S8	-	-	✓	-	-	✓	✓	✓
S9	-	-	✓	-	-	✓	✓	✓
S10	-	-	✓	-	-	✓	✓	✓

2.3.2 X-Ray Diffraction Analysis (XRD)

X-ray diffraction measurement of nanosilk was performed on the Angle dispersive XRD beamline (BL-12) of Indus-2 synchrotron source, RRCAT (India), using an image plate area detector (MAR345dif). The X-ray wave length (1.1 Å) used for the present study was accurately calibrated by doing X-ray diffraction on LaB6 NIST standard.

2.3.3 Morphological analysis of the nanocomposite films by FE-SEM microscopy

The morphologies of seven types of nanocomposite films (S1, S2, S3, S4, S5, S6, and S7) were carried out by using a field emission scanning electron microscope (SU8230) at an accelerating voltage of 5 and 10 kV. The samples were cut in the size of 5×5 mm in the rectangular shape and carbon was painted at the edge of the surface. The films were coated with a thin layer of Au for 45 sec prior to analysis (*Figure 2.5*).



Figure 2.5 Sample preparation (left), sputter coating (middle), and FESEM instrument (right)

2.3.4 ATR-FTIR spectroscopy

ATR-FTIR data collection was conducted on a Jasco FT/IR6300 equipped with an ATR PRO 470-H spectrometer. All spectra were measured using air as a background. A total of 25 cumulative scans were taken per sample with a resolution of 4 cm^{-1} , in the absorbance mode, in the frequency range of $4000\text{-}400\text{ cm}^{-1}$. The test was done at room temperature, in triplicates.

2.3.5 Differential Scanning Calorimetry (DSC)

Differential Scanning Calorimetry (DSC) measurements for the S1, S2, S3, S4, S5, S6, and S7 samples were carried out using Mettler Toledo DSC 3+ instrument under nitrogen purge (50 mL/min). The heating and cooling rates were 10°C/min . An initial mass of each sample was shown in the *Table 2.3*.

Table 2.3 Initial weight of DSC and TGA analysis

Sample code	Initial mass (mg)	
	DSC	TGA
S1	2.25	8.51
S2	2.10	8.90
S3	2.28	8.39
S4	2.94	9.67
S5	2.44	9.55
S6	2.19	7.22
S7	2.31	9.97

They were sealed in a standard aluminum pan (40 μL) (*Figure 2.6*). In this measurement a heat-cool-heat system was used and the second heating scan thermogram applied for thermal analysis. First, the sample was heated from 0 to 220°C to erase thermal history. Then, it was cooled down to 0°C before re-heating it to 220°C. The glass transition temperature (T_g) was obtained as the inflection point of the particular heat increment at the transition of the glass-rubber state.



Figure 2.6 DSC instrument (left) and aluminum sample pans (40 μL) covered with the lids (right)

2.3.6 Thermogravimetric Analysis (TGA)

The thermogravimetric analyses were carried out using Mettler Toledo TGA/DSC 3+. The S1, S2, S3, S4, S5, S6, and S7 samples were cut and placed into an experimental sample pans with a sensitive microbalance (*Figure 2.7*). A furnace was provided with nitrogen atmosphere at the rate of 50 mL/min, in the temperature range from 25 to 500°C. The heating rate was 10°C/min. The curves were plotted between percent of weight loss and temperature. The first derivative of the mass loss curves also were plotted against temperature (DTG).



Figure 2.7 TGA instrument (left) and reference and sample pans were on a sensitive microbalance (right)

2.3.7 Tensile tests of sample films

Tensile tests were performed on the INSTRON 3345 Tensile Tester. A length and a width of the strips of BC and SF containing nanocomposite films was 45 mm and of 15 mm, respectively. The applied cross-head speed was 5 mm/min on all five specimens of each samples (S7, S8, S9, S10).

2.3.8 Dynamic mechanical analysis (DMA)

DMA measurement of BC nanocomposite films (S7, S8, S9, and S10) was performed in shear mode on a METRAVIB DMA50 machine with a DYNATEST 6.9 software. Specimens were prepared to dimensions of approximately $2 \times 10 \times 0.034$ mm. First, frequency sweep was studied. The frequency of the loading was varied from 0.2 Hz to 20 Hz at room T. Temperature scans were run from -100 to 200°C at a heating rate of $3^\circ\text{C}/\text{min}$ with a frequency of 1 Hz. All samples were carried out under the white light illumination and measured the value of storage modulus (E') and loss tangent ($\tan \delta$). In case of S7, the light effect was investigated; therefore, it was stored in the dark for more than 12 hours and measured without any light.

2.3.9 Complex conductivity (Conductance) measurements

Four types of samples (S7, S8, S9, and S10) were used for measuring the conductivity at 2.4 kHz in the homemade cell and there were no contact with the

electrodes (*Figure 2.8*). Humidity was $40\pm 2\%$. For each sample, time dependent measurements in the dark and under illumination were also performed.



Figure 2.8 Photo of the home-made cell (Sopron University) used in photo-electrical characterizations of the films

Chapter III

Results and discussion

3.1 The effect of acid hydrolysis on BC and SF fibres

In this work, mild acid hydrolysis was used by application of conc. 37% HCl (fuming hydrochloric acid). This strong acid is completely ionized as shown in the *Figure 3.1*. The purpose of this process is to hydrolyze the fibres of treated-BC and degummed-SF into nanofibrils. In this study, fuming HCl acid was used at ambient temperature and performed inside the desiccator. We investigated the amount of acid used and weight the gain of BC and SF content. In each type of fibres, the average of weight was slightly increased (5.4% and 5.6% for BC and SF, respectively) after hydrolysis. Battista et al., 1950 revealed that the increasing weight of cellulose probably comes from a molecular layer of water bounded to the molecules of cellulose.

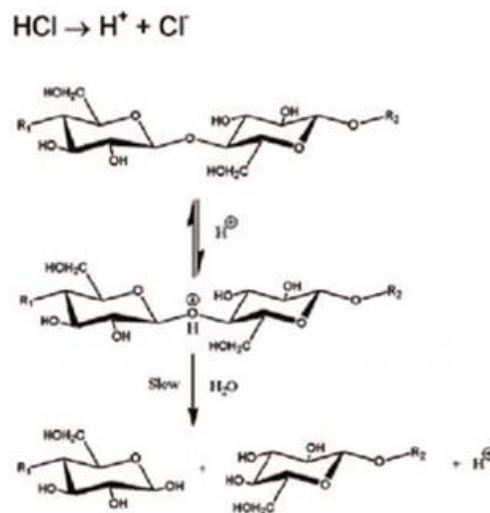


Figure 3.1 Mechanism of acid hydrolysis of cellulose fibres (Habibi, Lucia, & Rojas, 2010)

However, this hydrolysis induced the increasing of crystallization and could broken down the amorphous regions. Also, they claimed that the relatively mild condition for acid hydrolysis caused the crystal growth and the crystallization of long-chain segments because the small content of glycosidic bonds of cellulose chains was

broken in a slow rate. Therefore, these nanofibrillated BC provides superior thermal and mechanical properties. In case of hydrolyzed SF fibrils, several variables affect to the hydrolysis process, such as temperature, time, and hydrolysis agent (Fountoulakis & Lahm, 1998). Asquith et al., 1977 reviewed that acid hydrolysis caused main chain fission of polypeptide chains and occurred throughout the proteins in a random manner. Each of peptide bonds will be decomposed and result in amino acids (“The hydrolysis of proteins”, 2016). Nadiger et al., 1985 confirmed that after acid hydrolysis process, the composition of silk fibroin mainly comprised of glycine, alanine, and serine about 80%.

3.2 Films characteristics

Comparison of self-standing dried samples transparency with the thickness in the range of 0.13-0.5 μm is illustrated in *Figure 3.2*. All films exhibited different levels of transparency but visually seemed homogenous with no bubbles, could be simply removed from the plate and were flexible. The greatest clarity was shown by films of pure PVA and PVA-AgNC (S3 and S6). In contrast, the films containing BC (S1, S4, S7, S8, S9, and S10) displayed decreased transparency. Generally, the pristine BC dried film exhibited light-brownish color owing to the applied heat during drying step. Moreover, the 3-D network structure of BC nanofibrils has air interstices in between. Hence, the interface between the air interstices and the cellulose fibrils caused the light diffraction, then the opacity.

However, the size of the material is associated with the light wavelength which can be explained by this equation:

$$x = (\pi \cdot D) / \lambda$$

Where x is the size parameter of a solid material, D is referred to diameter of material (nm), and λ is the wavelength of light.

In this study, wavelength of visible light (380-780 nm) was used to calculate. The average diameter of BC nanofibrils is 80 nm. Hence, the size factor was considered to be 0.314 to 0.628. For this reason, BC film presents almost free from light scattering according to Rayleigh scattering as shown in *Figure 3.3* (Linder, 2014,

Ummartyotin, Juntaro, Sain, & Manuspiya, 2012 and Ougiya, Watanabe, Matsumura, & Yoshinaga, 1998).

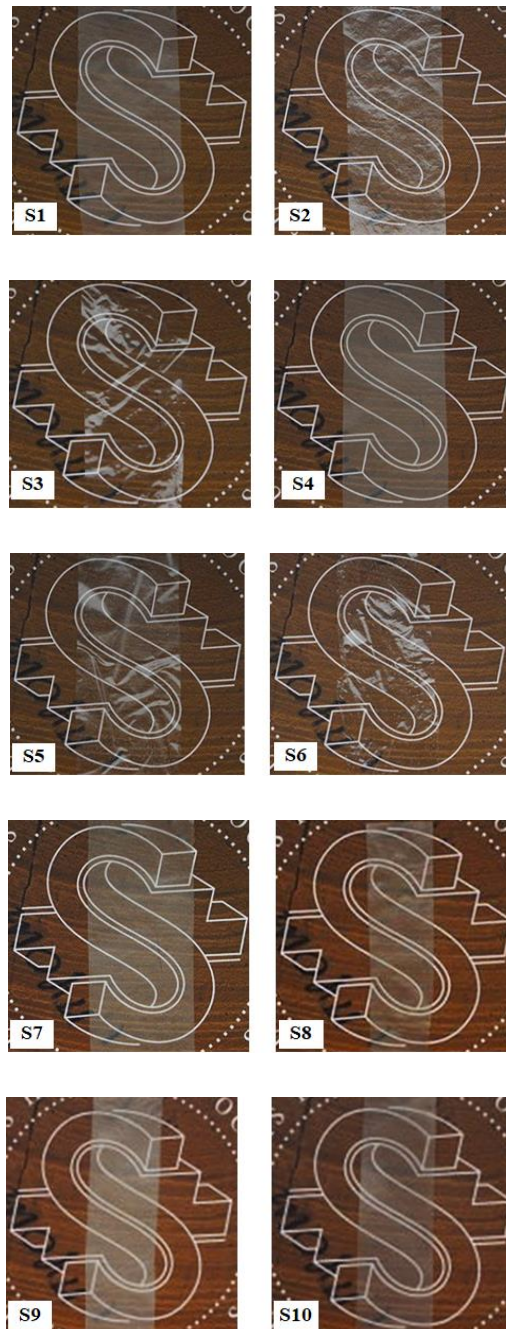


Figure 3.2 Optical images of transparent films of BC-PVA (S1), SF-PVA (S2), PVA (S3), BC-PVA-AgNC (S4), SF-PVA-AgNC (S5), PVA-AgNC (S6), BC-SF-PVA-AgNC (S7), BC-SF (S8), BC-SF-AgNC (S9), and BC-SF-PVA (S10) placed on a bookcover

In contrast to silk fibroin film itself produced high-quality optical film with great transparency and reduce scattering. But in this work, the SF fibrils have an average

10.75 μm in diameter. Therefore, it can calculate the size parameter to be 21.1 to 42.2. It shows in the range of Cylinder scattering.

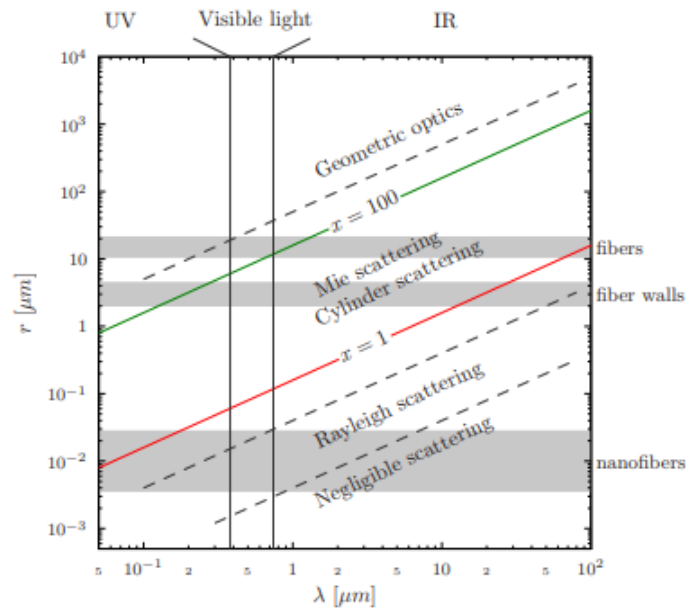


Figure 3.3 Scattering regimes between wavelength (x-axis) vs particle size (y-axis) (Linder, 2014)

Regarding PVA, the excellent film-forming, is one type of synthetic polymer and water-soluble. It can generate white or colorless dried film as can be clearly seen in the *Figure 3.2* (S3). In this study, according to the high transparency of PVA blending with BC and SF can cause these films much more transparent optically. It could be mention that after BC and SF blended with PVA solution, the film formed homogenous structure during drying process. Therefore, S1, S2, S4, S5, S7, and S10 show clear and transparent films. In this present work, the addition of PVA polymer which has refractive index (RI) very close to bacterial cellulose (approximately 1.618 along the fiber and 1.544 in the transverse direction), exhibit transparent film because of the restriction of the light diffraction at the interface between PVA and fibrils according to other researchers' findings (Ummartyotin, Juntaro, Sain, & Manuspiya, 2012 and Nogi & Yano, 2008). In the case of SF film, it can be explained by the lower fiber content of SF than the amount of PVA. Therefore, the effect of SF does not occur and present very clear film. However, the transparency of the AgNC containing films (S4, S5, S6, S7, and S9) remained unchanged.

3.2.1 Optical transmittance

The optical transmittance in the visible region (380-780 nm) of the electromagnetic spectrum is presented in *Figure 3.4*. The results of our samples (S2, S3, S5, and S6 films), was compared to the result for PE. The best transparency of all films was found for S3 and S6 showing notable transmission (transmittance between 78-80%) across the visible spectrum. According to this fact, these samples can be considered transparent. In case of S2 and S5, moderately transparent films were produced with 10-20% transmission.

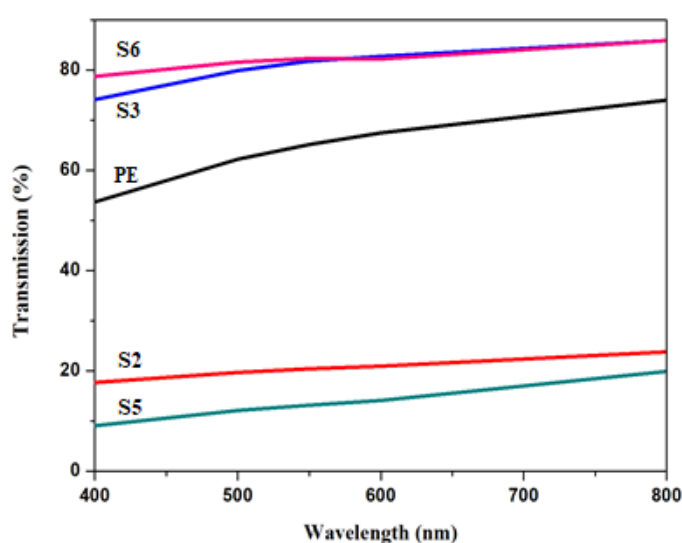


Figure 3.4 Transmittance versus wavelength graph for Polyethylene (PE), SF-PVA (S2), PVA (S3), SF-PVA-AgNC (S5), and PVA-AgNC (S6) substrates

This could be explained by the protein's chemical components that mainly comprise of Ser, Gly, and Ala amino acid in its sequence. These amino acid residues in protein exhibit weak absorption in the spectra range of 400-1200 nm (Liu et al., 2014). Furthermore, silver nanocubes did not affect their intrinsic optical properties. On the other hand, bacterial cellulose containing samples showed the translucent look due to the transmittance less than 2% (not presented in this Figure) as experienced by Jung et al., 2008. This is probably due to the high BC fiber content and the size of BC fibrils. In this work, instead of using pure nanocrystalline BC for fabricating flexible BC film, microfibrillated BC was used for making the film strong enough to peel from the support after oven-drying. Moreover, the nanosized BC filled the vacancies of the BC microfibrils network. The poor transparency can be ascribed to microfibrillated

BC content and partially miscible with PVA which makes the film scatter light and be more opaque.

3.2.2 Transparent and flexible electronic display standard

The regulation of organic light emitting diode display is exhibited as ANSI/UL 8752 – CAN/ULC-S8752. It is a bi-National Standard between United State and Canada which was updated on the 1st of February 2012. It covers OLED luminaires and OLED panels integral to other luminaires. It is indicated only for glass substrate; no sharp edges, minimum thickness or test for weight of broken pieces, mounting secureness test (“Lighting”, 2013). However, there are some other requirements for flexible substrate such as glass and plastic (Polyethylene naphthalate or Polyimide). Normally, the thickness is around 100 μm (*Table 3.1*), in contrast to our samples which present less than 0.5 μm (“Flexible Electronics: Materials and Applications”, 2009). Also, the specific weight of our samples is greatly smaller than the one for glass and plastic substrates. As shown in the visually transparent property, all of our films also performed very high transparency.

Table 3.1 Types and properties of flexible displays

Sample code	Thickness (μm)	Weight (g/m^2)	Safe bending radius (cm)	Visually transparent Yes/no or slightly	Elastic modulus (GPa)	Permeable to oxygen, water vapor	References A or B
Glass (1737)	100	250	40	Yes	70	No	A (“Flexible Electronics: Materials and Applications”, 2009)
Plastic (PEN, PI)	100	120	4	Slightly	5	Yes	A
ITO-SiO ₂ -BC	0.185	n/a	n/a	Slightly	n/a	Yes	B (Legnani et al., 2008)

3.3 Field Emission Scanning Electron Microscope analysis (FESEM)

The characteristic FESEM images of dried bacterial cellulose modified with silk fibroin protein, polyvinyl alcohol, and silver nanocubes film (S7), silk fibroin blended PVA film (S2), and pure PVA film (S3) which were performed at 5 and 10 kV are shown in *Figure 3.5a*, *3.5b*, and *3.5c*, respectively. The surface of this dried film obviously presents a 3-D fibrous ultrafine network structure (*Figure 3.5a*). The BC nanocrystalline fibrils diameters were found the average less than 100 nm, labeled with yellow color. Also, many pores were filled with silk fibroin and PVA matrix with the diameter size in the range of 30 to 182 nm. The nanoscopic view of the film surface did not present any bacterial skeletons and/or other impurities. It can be clearly observed in *Figure 3.5b* that pure SF modified with PVA film also exhibited SF highly porous 3-D network structure and fibrils with higher average diameters than that of BC. It shows around 7.5 to 14 μm and the length is more than 100 μm . However, the surface skin of silk fibroin fibrils was rather smooth. The addition of PVA scarcely had an effect on the fibrils surface. Moreover, it shows separate phases between silk fibroin fibrils and PVA polymer in contrast with BC-SF-PVA-AgNC film. It is implying that PVA can well-penetrated to the BC-SF fibrils than SF-PVA blend film. Since the poor interaction between SF and PVA polymer occurs from PVA crystallization or the aggregation of SF molecular chains (Ling, Qi, Knight, Shao, & Chen, 2013). However, this film still presents very high transparency by naked-eye, and possess good flexibility. It can be seen in *Figure 3.5c* that pure PVA film has smooth and homogeneous surface because of its excellent film-forming properties.

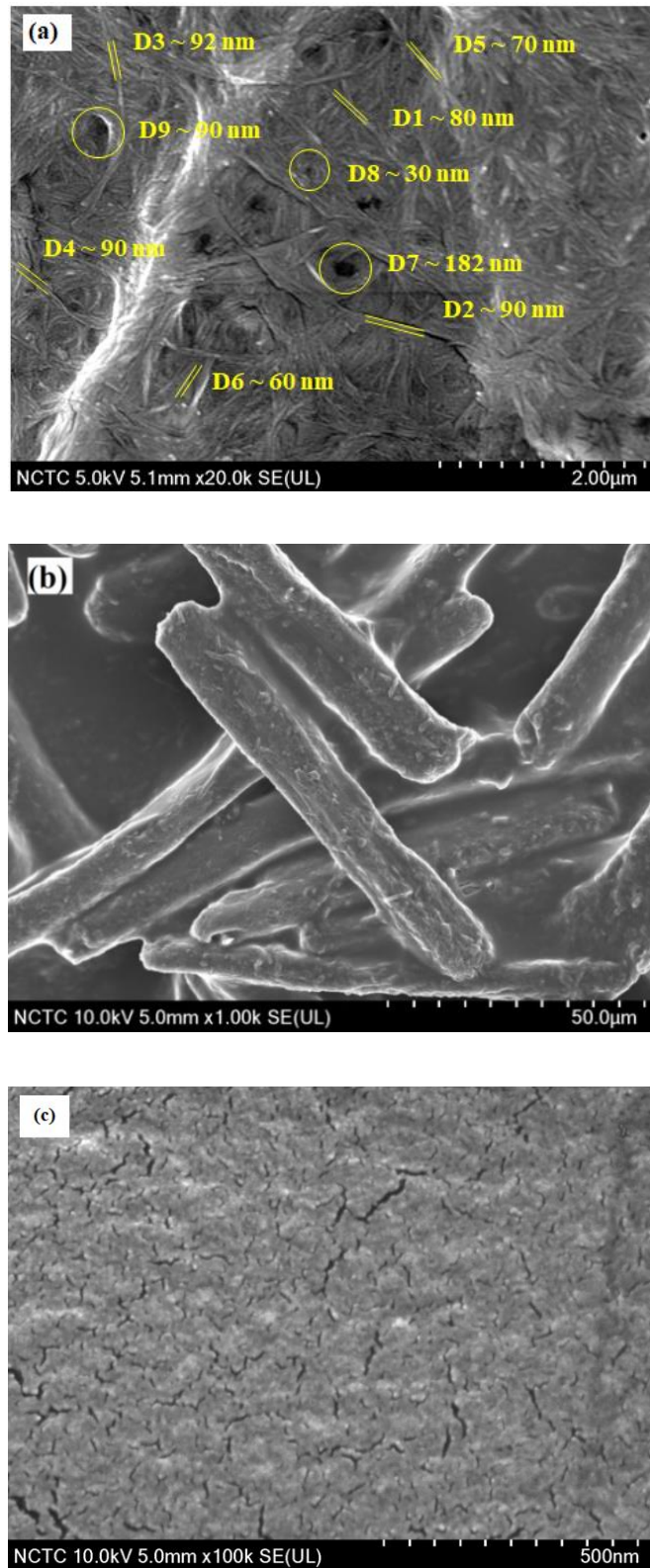


Figure 3.5 FESEM images of BC-SF-PVA-AgNC (S7) (a), SF-PVA (S2) (b), and pure PVA film (S3) (c)

As displayed in *Figure 3.6a*, it can be clearly observed that most of silver nanocubes, synthesized by an illustrious polyol process, can be well characterized by predominantly nanocube shapes with only some nanospheres. *Figure 3.6b* shows a representative typical images of AgNC. The width was found between 180-200 nm and the length was shown from 160 to 200 nm. In this sample, it shows the phase separation between SF and AgNC. *Figure 3.6c and 3.6d* display better uniform distribution and no aggregation of AgNC compared to SF-PVA film. It suggests that PVA was a good dispersant.

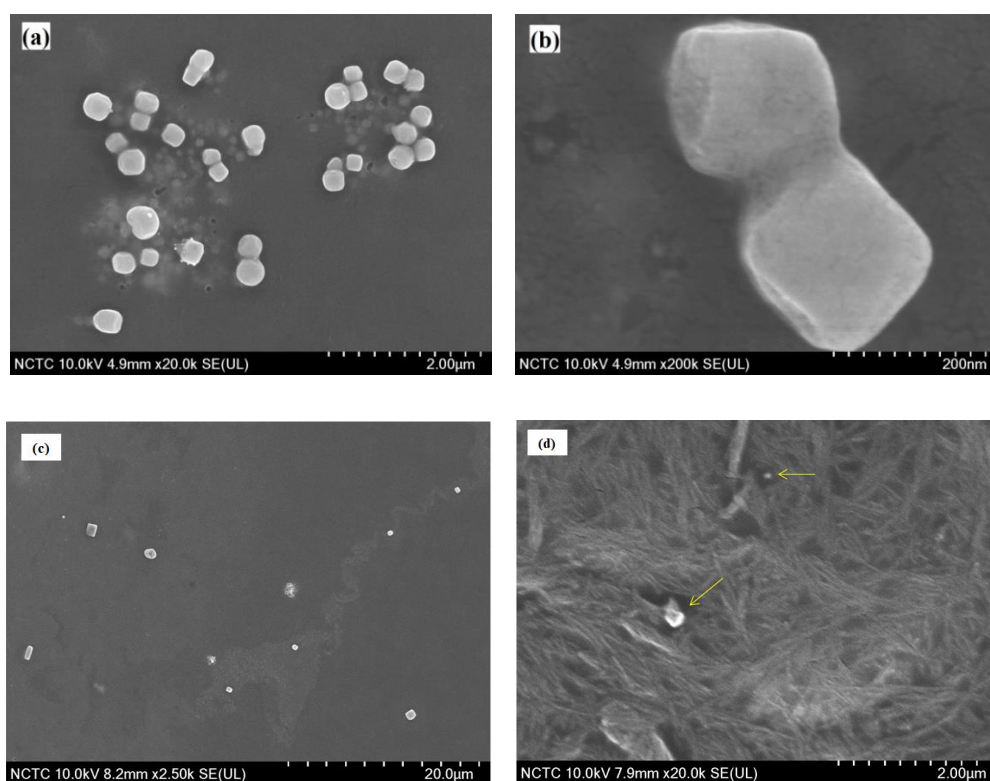


Figure 3.6 FESEM images of the distribution of silver nanocubes embedded in SF-PVA film (S5) (a), the size of the isolated silver nanocubes (b), PVA-AgNC film (S6) (c), and BC-SF-PVA-AgNC film (S7) (d), the yellow points indicate the AgNC

3.4 Angle Dispersive X-ray Diffraction (ADXRD)

Angle Dispersive X-ray Diffraction (ADXRD) of nanosilk was presented in *Figure 3.7*. It is a non-destructive tool for the study of crystalline structure which affects many properties in solid state (Um, Kweon, Park, & Hudson, 2001).

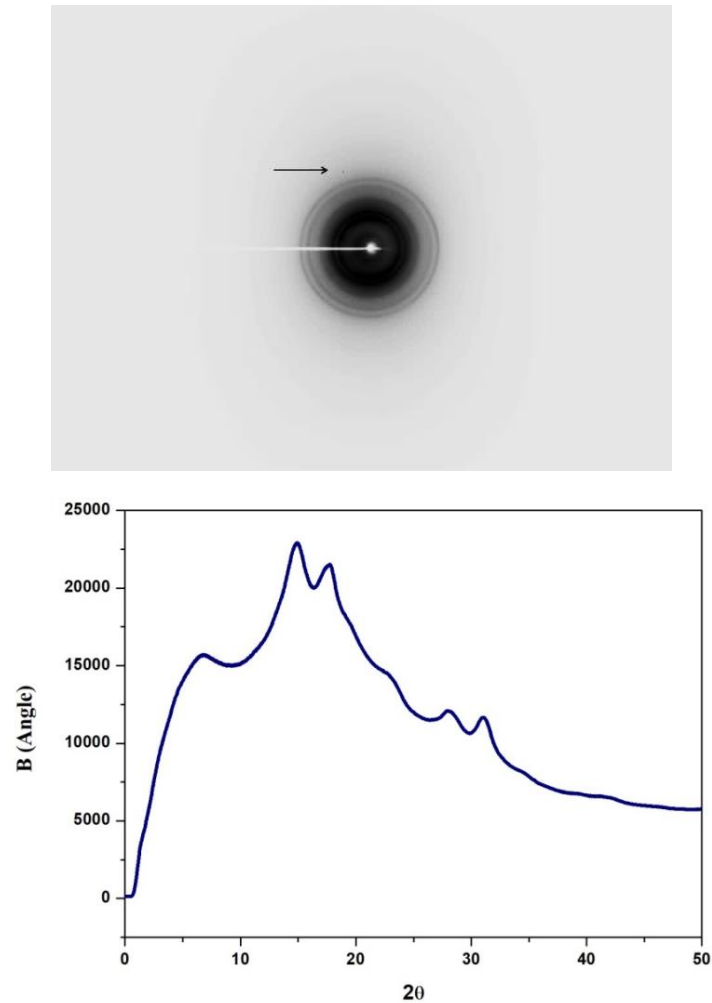


Figure 3.7 Diffraction peaks of nanosilk

In our study, nanosilk structure was observed after hydrolyzed by fuming acid. It exhibited a major diffraction peak at 14.9° and five minor peaks at 6.9° , 17.7° , 24.6° , 28° , and 31.1° , respectively, corresponding to the 4.24, 9.14, 3.57, 2.58, 2.27, and 2.05 Å spacing, respectively. The crystalline structure of SF was affected by solvent or treatment agent (Um, Kweon, Park, & Hudson, 2001). Similar to Um et al., 2001, they found that SF treated in water formed amorphous state (0% crystallinity calculated from XRD curve). This can be concluded that silk fibroin can present also amorphous state.

3.5 Attenuated total reflectance Fourier transform infrared spectroscopy

The attenuated total reflection (ATR) technique is the most widely used technique for infrared spectroscopy to examine the surface properties of materials (Kljun et al., 2011). Our BC containing samples of S7-S10 (BC-SF-PVA-AgNC, BC-SF, BC-SF-AgNC, and BC-SF-PVA) films were prepared to study the interaction within the structures. The obtained spectra from ATR-FTIR analysis in the region of 4000-400 cm^{-1} exhibited the structure of BC, SF, PVA, and AgNC films. That evidenced by the pictures showed in *Figure 3.8* and the data in *Table 3.2*. In our study, all types of samples, the spectra were corresponded to the main characteristics of bacterial cellulose and some peaks of silk fibroin protein. It was also noticed that when cellulose was blended with silk fibroin protein, the conformation of protein would have changed. The band at 3400 cm^{-1} shows decreasing intensity when the BC was blended with SF and PVA. This is implying that the hydroxyl group of BC and PVA was related in the reaction. Moreover, at 3285 cm^{-1} shows a broad peak corresponding to the BC stretching vibrations of inter-hydrogen bonding. So the intermolecular H-bonds between OH groups of BC cellulose and NH in the amide groups of SF formed, in contrast with a decrease in intramolecular H-bonds of cellulose.

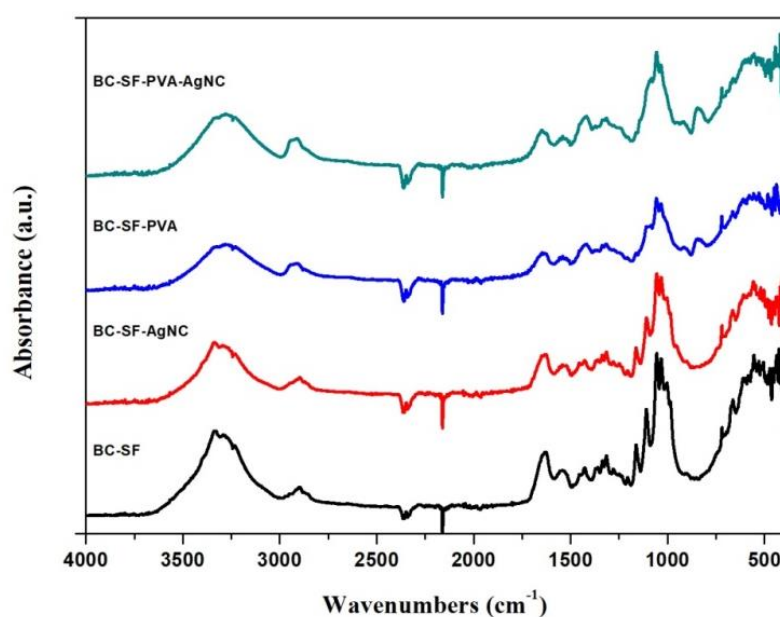


Figure 3.8 FT-IR spectra of BC-SF-PVA-AgNC (S7), BC-SF (S8), BC-SF-AgNC (S9), and BC-SF-PVA (S10) films

Table 3.2 Spectral characteristics at various wavelengths for BC-SF-PVA-AgNC (S7), BC-SF (S8), BC-SF-AgNC (S9), and BC-SF-PVA (S10) films

Wavenumbers (cm ⁻¹)	Band Assignment	References
3400	O-H stretching vibration of intra-hydrogen bond	(Y Hosakun, 2017 and Oliveira Barud et al., 2015)
3285	O-H stretching vibration of inter-hydrogen bond	(Y Hosakun, 2017 and Tsalagkas, 2015)
2900	C-H stretching of CH ₂ and CH ₃ groups	(Y Hosakun, 2017 and Tsalagkas, 2015)
1635	C=O stretching (peptide backbone of amide I)	(Hofmann et al., 2006)
1540	N-H bending vibration bond (peptide backbone of amide II)	(Y Hosakun, 2017 and Hofmann et al., 2006)
1263	C-N stretching (peptide backbone of amide III)	(Y Hosakun, 2017 and Hofmann et al., 2006)
1170	C-O-C asymmetric stretching vibration	(Y Hosakun, 2017)
1110	C-O-C nonsymmetric in-phase ring vibration	(Oliveira Barud et al., 2015)
1055	C-O symmetric stretching of primary alcohol	(Oliveira Barud et al., 2015)
898	β-glucosidic bonds between the glucose units	(Oliveira Barud et al., 2015)
850	C-C stretching	(X. Han, Chen, & Hu, 2009)
400-700	O-H bending	(Y Hosakun, 2017 and Hofmann et al., 2006)

This present work also shows the characteristic of β -sheet of silk fibroin structure. Therefore, this strong intensity of the β -sheet peaks proves the presence of the crystalline silk fibroin protein (Oliveira Barud et al., 2015). In addition, the characteristics of random coil conformation and α -helix (silk I) absorption peaks are disappeared similar to Yang et al., 2000 results after they blended cellulose with silk fibroin. They observed that β -sheet conformation was the result of the formation of intermolecular hydrogen bonds between cellulose and silk fibroin protein by blended SF with cellulose. When AgNC was blended (BC-SF-AgNC and BC-SF-PVA-AgNC), no new peaks were noticed other than common characteristics peaks of BC and SF nanofibrils. It probably can be concluded that obscurity of silk II characteristics made the peak of AgNC disappeared and AgNC did not affect the native structure of the film. All of major peaks showed similar to BC-SF and BC-SF-PVA films but they shifted to wider bands.

3.6 Differential Scanning Calorimetry (DSC)

Differential Scanning Calorimetry (DSC) is a technique for analysing thermal properties of material. It was used as an equipment to characterize the difference in heat flow between the reference and the sample as a function of temperature. Also, it can be used to measure glass transition temperature (T_g) and melting temperature of crystallized region (T_m) in the material. T_g indicates the mechanical properties of polymer when it transforms from glassy state to rubbery state. At temperatures above T_g the polymer chains have high energy to undergo crystallization. In case of T_m , the polymer can move around freely at this temperature and hence it is not in ordered arrangement. Also, changes of specific heat capacity (ΔC_p) was investigated. It represents the amount of energy that needed to increase the temperature of one gramm of sample by one degree temperature.

Figure 3.9 shows the DSC thermograms of S1, S2, S3, S4, S5, S6, and S7 samples.

The characteristic temperatures are tabulated in *Table 3.3*.

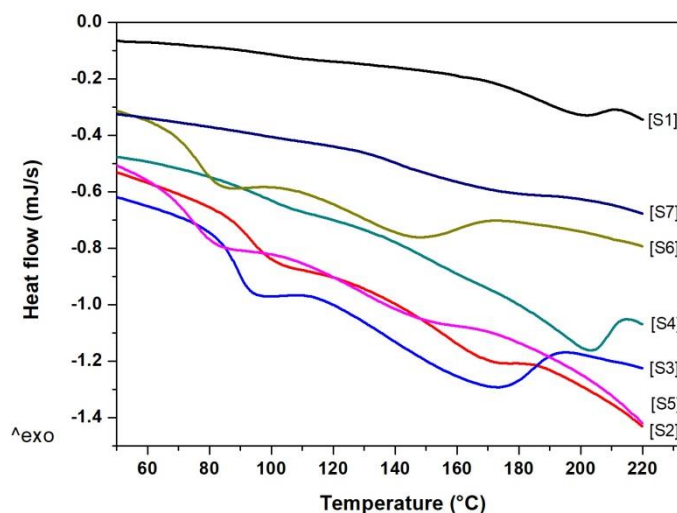


Figure 3.9 DSC second heating curves of BC-PVA (S1), SF-PVA (S2), pure PVA (S3), BC-PVA-AgNC (S4), SF-PVA-AgNC (S5), PVA-AgNC (S6), and BC-SF-PVA-AgNC (S7) at heating rate of 10 K/min

Table 3.3 Differential Scanning Calorimetry Results of seven samples

Sample No. and composition	T_g (°C)	T_m (°C)	ΔH (J/g)	ΔC_p (J/g·deg)
S1 (BC-PVA)	101.07	199.00	2.68	0.11
S2 (SF-PVA)	94.81	167.50	4.43	0.49
S3 (pure PVA)	88.69	169.50	21.51	0.60
S4 (BC-PVA-AgNC)	105.10	202.50	7.57	0.09
S5 (SF-PVA-AgNC)	76.41	147.33	3.00	0.49
S6 (PVA-AgNC)	77.14	145.33	9.17	0.57
S7 (BC-SF-PVA-AgNC)	n/a	166.67	3.75	n/a

The glass transition temperature (T_g) of all samples showed as single temperature and shifted from 88.69 °C for pure PVA (S3) to 101.07, 94.81, 105.10, 76.41, and 77.14 °C for S1, S2, S4, S5, and S6, respectively. The addition of BC (S1) increased the T_g of pure PVA. It could be described by the competitive interactions between the surface of BC, PVA, and water in the atmosphere. This phenomenon is owing to restriction of the segmental mobility of PVA chains in the interfacial zone, called relocalization effect. According to hydrophilic behaviour of both the BC and PVA, they are extremely miscible and thus the formation of strong hydrogen bond between the BC and PVA matrix was assumed. A similar result was reported on

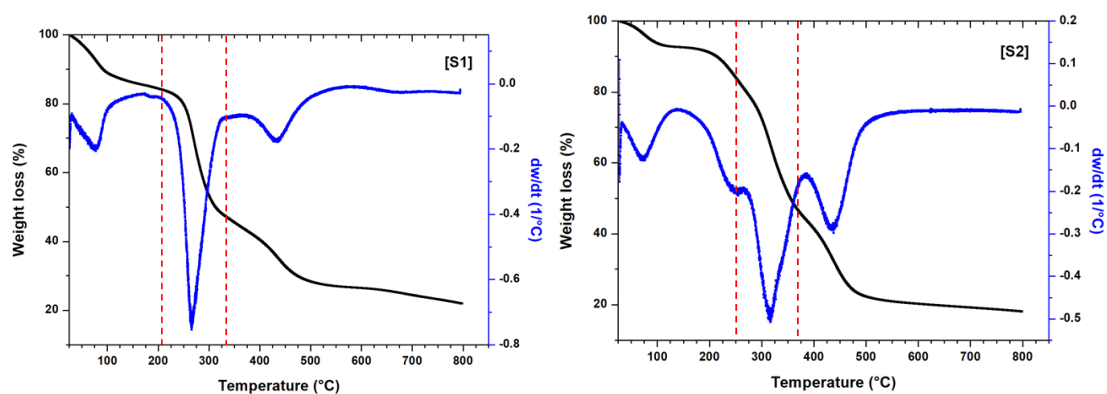
cellulose whiskers from cotton linter mixed with PVA (Roohani et al., 2008). Also in the case of S2, the T_g are shifted to higher value compared to S3. This is associated with the partially crystalline structure of the PVA with the physical and chemical characteristics such as hydrogen bond between hydroxyl groups from inter- and intra-chain interaction. Also, Ling et al., 2013 claimed that the blending of SF and PVA were incompatible investigating from FESEM images as mentioned above (Ling, Qi, Knight, Shao, & Chen, 2013). This behaviour could be described by the change of the crystal form when PVA was embedding by SF in high content (Luo, Chen, Hao, Zhu, & Zhou, 2013). Luo et al., 2013 studied the thermal effect on the ratio of SF:PVA films. They observed that when the ratio of SF:PVA was reached 30:70 and 40:60, the endothermic peaks were broaden showing better thermal stability. When silver nanocubes were integrated into the samples (S4, S5, and S6), the T_g of S5, and S6 were shifted downwards from S2 and S3, respectively but T_g for S4 was higher than S1. For S7, the glass transition peak was unrecognizable but it can be detected by DMA analysis. Only the endothermic peak appeared at 166.67 °C. This fact suggests the highly crosslinked structure of the substances. This means that the molecular structure of this S7 sample is compact and stiff confirming the crystalline structure (“The Glass Transition”, 2018).

The melting endotherm at T_m of all films is also listed above in *Table 3.3*. The T_m of BC-PVA (S1) was increased after incorporation AgNC into it (S4) and showed the highest melting point (202.50 °C). On the other hand, S3 and S5 presented lower T_m than S6 and S2, respectively. These differences in behaviour suggest stronger interaction between BC, PVA, and AgNC in sample S4. Regarding to S7, the T_m is nearly similar to S2.

3.7 The thermogravimetric (TGA) and derivative thermogravimetric (DTG) analyses

The TGA and DTG (dw/dt) curves to show thermal degradation of S1, S2, S3, S4, S5, S6, and S7 samples are depicted in *Figure 3.10*. Corresponding data can be found in *Table 3.4*.

According to TGA curves, the small weight losses presented below 100 °C in Region I. refer to the evaporation of absorbed water. The maximum values (32-61%) in weight loss of S1, S2, S3, S4, S5, S6, and S7 are clearly exhibited in Regions III., IV., III., II., III., II., and II., respectively. In Region I. the highest percentages in weight loss temperature were shown by S1 and S7 samples (13.2%, 13.4%), and these samples started to degrade earlier, at lower temperature (25.7 °C) than the others (27.3-27.4 °C). This can be explained by the highly hydrophilic properties of BC. These samples can absorb more moisture from the atmosphere during preparation of the films for testing than the others. Obviously, the thermal degradation behaviour showed that the samples containing bacterial cellulose (S1, S4, and S7) initiated degradation below 206 °C for the major weight loss. Regarding the maximum temperature of DTG peak, it is indicated that glycosidic linkages of cellulose were cleaved at lower temperature than the degradation temperature of native cellulose (about 400 °C). This behaviour can be explained by the effect of acid hydrolysis on structural changes in bacterial cellulose during film preparation. Li et al., 2012 claimed that when the numbers of free hydroxyl groups were increased by decreasing the size of cellulose (smaller polymeric degree), the degradation temperature would shift to a lower temperature range. This means that the size of bacterial cellulose (nano-size) affected the degradation temperature. The main degradation temperature is close to the one of pure PVA which began at 240 °C and followed by 281.5 °C to explain the PVA polymer backbone decomposition and chain scission (Li, Yue, & Liu, 2012). This means that PVA caused the BC to degrade at lower temperature and also, BC induced the PVA to have thermal stability. However, this composite material still have good thermal stability.



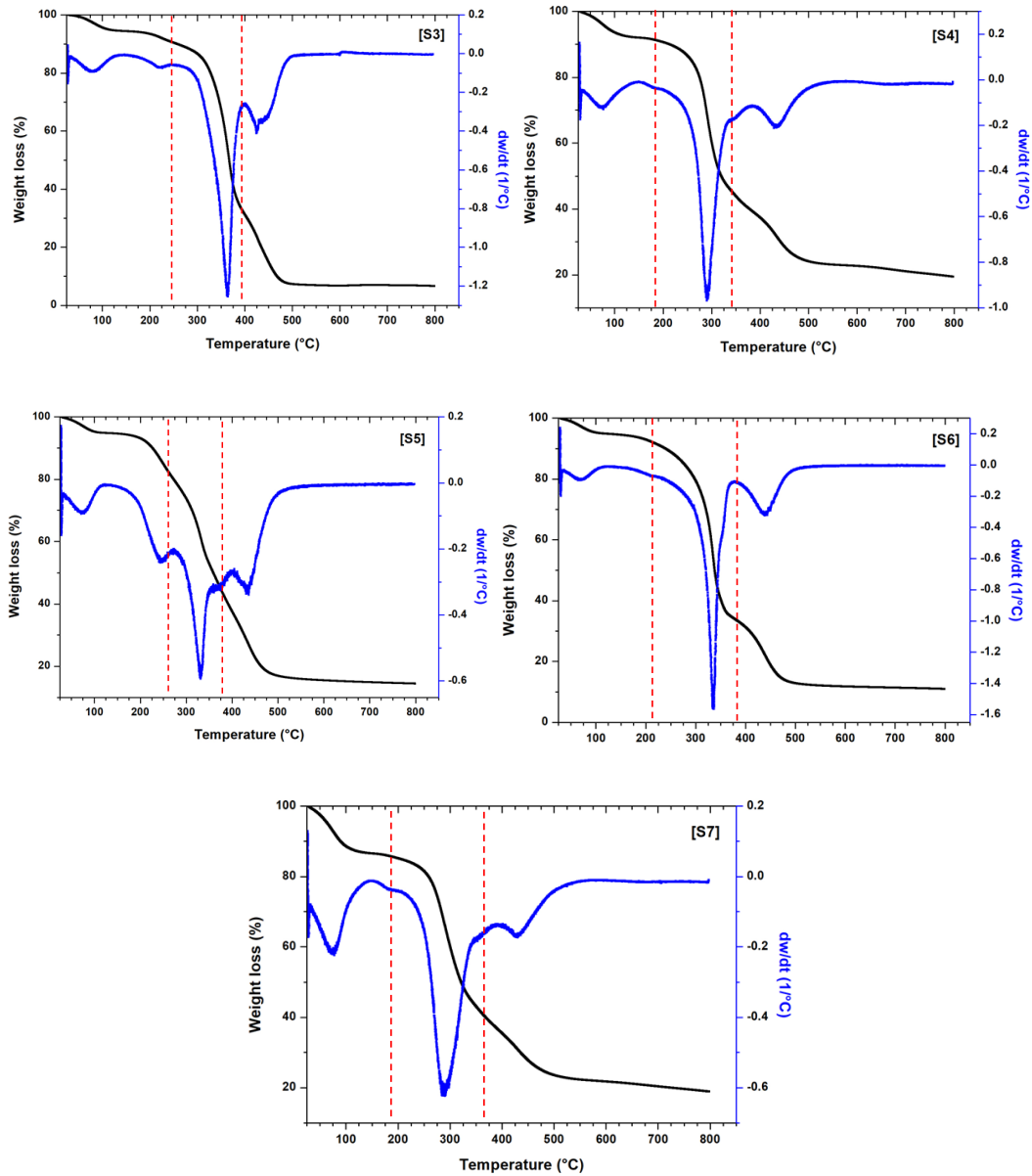


Figure 3.10 TGA (black) and DTG (dw/dt) (blue) curves of samples (S1) BC-PVA, (S2) SF-PVA, (S3) pure PVA, (S4) BC-PVA-Ag, (S5) SF-PVA-Ag, (S6) PVA-Ag, and (S7) BC-SF-PVA-Ag

Table 3.4 Degradation temperatures of samples S1, S2, S3, S4, S5, S6, and S7 determined from TGA and DTG results

TGA and DTG curves		S1	S2	S3	S4	S5	S6	S7
Region I.	Temperature range, °C	25.7-137.6	27.3-126.7	27.4-167.8	27.4-191	27.3-140	27.3-217.5	25.7-175.7
	Peak, °C	75	72.5	82.7	76.6	80	79.8	80
	Weight loss, %	13.2	7.4	5.8	7.9	5.4	5.2	13.4
	Temperature	137.6-	126.7-	167.8-	191-	140-	217.5-	175.5-

Region II.	range, °C	205	198	243.9	346	238.9	377	374.9
	Peak, (°C)	162	189.9	212	290	200	336.6	290.1
	Weight loss, (%)	2.6	0.1	4.6	52.3	15.6	61	50.6
Region III.	Temperature range, °C	205-325.8	198-250	243.9-386.8	346-514	238.9-375.1	377-510	374.9-575
	Peak, (°C)	265.9	242	364.6	440	331.7	439.6	442
	Weight loss, (%)	38.8	11.3	59.1	16.1	32.4	21.3	13.9
Region IV.	Temperature range, °C	325.8-625	250-372	386.8-432	n/a	365.1-402.8	n/a	n/a
	Peak, (°C)	436.7	316.45	421	n/a	388	n/a	n/a
	Weight loss, (%)	19.2	36.8	9.3	n/a	10	n/a	n/a
Region V.	Temperature range, °C	n/a	372-530	432-518.1	n/a	402.8-512.3	n/a	n/a
	Peak, (°C)	n/a	438	453	n/a	440	n/a	n/a
	Weight loss, %	n/a	22.1	14.2	n/a	20	n/a	n/a
Residue, %		26.2	22.3	7	23.7	16.6	12.5	22.1

In case of samples S2, S3, and S5, five steps of degradation can be seen. Each sample shows significantly different behaviour. For example S2 in Region III had only 11.3% weight change at about 200 °C on the TGA graphs. This ascribes that the endotherm peak around 200 °C could be considered as a physical transition such as melting of PVA crystals. The major initial weight loss was found in temperature range of 250-372 °C after the evaporation of water. The maximum mass loss (36%) of the film was presented at 316.5 °C. This can be connected to the breakdown of silk fibroin amino acid chains, the effect of the overlapping between the changed β -structure of silk fibroin and PVA polymer backbone thermal decomposition (Luo, Chen, Hao, Zhu, & Zhou, 2013). However, this sample has higher thermal stability than S1. For pure PVA (S3), the main mass loss was occurring due to chain scission reactions of PVA chain. According to the PVA structure, it has many OH groups that could be broken as water by heating and formed the conjugated polymers with polyene structures (*Figure 3.11.a*). Then other reactions occurs such as chain breakage resulted in aldehydes and ketones (*Figure 3.11.b, c*) (H. Yang, Xu, Jiang, & Dan, 2012). Nevertheless, high temperature (above 520 °C) destroyed the PVA main chains, caused decomposition, and resulted in the huge mass loss.

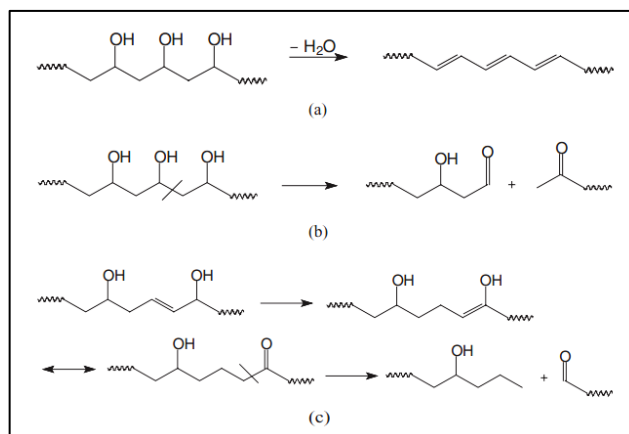


Figure 3.11 Changes in main chain of PVA reactions under heating (H. Yang, Xu, Jiang, & Dan, 2012)

In Region II., S4, S6, and S7 began to decompose earlier compared to another samples. In *Figure 3.10* increasing in thermal stability can be seen when silver nanocubes are present in the BC, SF, and PVA films (S4, S5, S6, and S7) in contrast to S1, S2, and S3. It is noteworthy to mention that AgNCs have higher thermal stability than polymeric chains of the films and the mobility of polymeric chains were reduced by weak intermolecular crosslink between AgNCs and OH groups of BC and PVA. For this reason, the mobility was restricted, hence caused the shift to higher temperature of decomposition (Juby et al., 2012). Moreover, S7 exhibited the widest temperature range with almost the maximum weight loss (175-375 °C, 50.6%). This can be described by an overlap of multiple peaks. Therefore this sample can well resist to high temperature. In case of S1 and S3, the maximum weight loss shows significantly higher values when embedded with AgNC (S4 and S6, 52% and 61%). On the other hand, AgNC obviously has caused reduced weight loss in sample S5 (32.4%) compared to sample S2 (36.8%). The final residues of all films presented in the last row of *Table 3.4*. The latter decomposition step is related to the decomposition of carbonaceous matter (above 325 °C). At the last temperature stage, the samples containing BC had greater amount of remaining residue than others. All of our samples did not fully decompose at temperature of 800 °C. For S1, it shows the highest residue (26.2%), in contrast to S3, which presented the smallest residue (7%). Even though, SF containing samples (S2 and S5) had 5 stages of decomposition,

however, they still have high amount of residue. For S4 and S5, even they started to decompose at lower temperature than S1 and S4, but they showed higher mass loss.

3.8 Tensile strength

In this study, the mechanical properties of all films containing SF [BC-SF-PVA-AgNC (S7), BC-SF (S8), BC-SF-AgNC (S9), and BC-SF-PVA (S10)] were investigated by using tensile tester. The results of these samples can represent the interactions between BC, SF, PVA, and AgNC. Tension was applied to a sample while measuring the applied force and the elongation. The stress-strain curves of these films were determined as shown in *Figure 3.12* and *Table 3.5*.

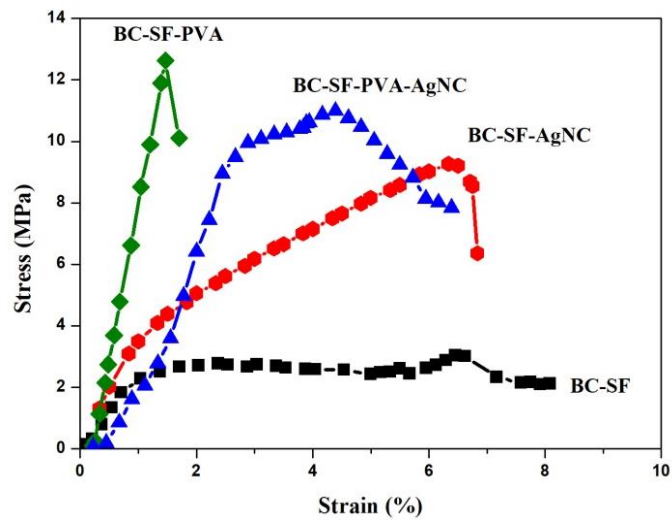


Figure 3.12 Stress vs Strain curves of BC-SF-PVA-AgNC (S7), BC-SF (S8), BC-SF-AgNC (S9), and BC-SF-PVA (S10) films

Table 3.5 Mechanical strength of BC-SF, BC-SF-AgNC, BC-SF-PVA, and BC-SF-PVA-AgNC films

Sample code and composition	Elongation at break (%)	Tensile strength (MPa)
S7 - BC-SF-PVA-AgNC	6.4	11.0
S8 - BC-SF	8.7	3.0
S9 - BC-SF-AgNC	6.8	9.3
S10 - BC-SF-PVA	1.7	12.6

The curve of BC-SF (S8) showed tensile strength of 3.0 MPa. While, tensile strength of BC-SF-PVA (S10) is approximately 3 times higher than BC-SF whereas the elongation is reduced to 8 times less. On the other hand, BC-SF-AgNC (S9) and BC-SF-PVA-AgNC (S7) shows not considerable different of both tensile value and elongation. It can be assumed that in this work, the ratio of BC/SF blending film (70:30) gives the opportunity of producing strong intermolecular interactions of hydrogen bonding as mentioned earlier. It encouraged β -sheet conformation of silk fibroin formation, and the changes in silk fibroin protein structure, confirmed by FTIR results, and increases the ability to react elastically to an applied force. In comparison of S10 and S7, the latter exhibited the great in elongation and also exhibited a significant higher value in tensile strength, hence, it can be implied that the AgNC affected the mechanical properties. The improved mechanical properties of this film could be due to the excellent mechanical performance and the ductility of silver nanocubes. However, S7 and S9 sample films containing AgNC showed very good tensile and elastic properties (11.0-9.3 MPa and 6.4-6.8%, respectively). In case of S10, it can be seen that the improved tensile strength showed significantly highest value (12.6 MPa) compared to S7, S8, and S9. This can be explained by the H-bonds interaction between BC, SF and PVA that as a matrix of this film.

3.9 Dynamic mechanical analysis (DMA)

Dynamic Mechanical Analysis (DMA) is a widely used technique to characterize the properties of the materials as a function of temperature, time, frequency, stress, press or an integration of these parameters. It was performed to study the viscoelastic characteristics and complex modulus of the samples by applying a sinusoidal stress and evaluating the change of strain. Dynamic mechanical analysis

revealed that the silver nanocubes in the BC-SF and BC-SF-PVA films have different effect on the film properties. *Figure 3.13* shows the storage (E') and loss (E'') shear moduli of all four films as a function of temperature (usually, the shear modulus is denoted by G but we used E to avoid ambiguity, since the conductance is also denoted by G , which will be explained later). It can be seen that after incorporation of AgNCs to BC-SF film, storage modulus significantly increases and the shape of both E' - and E'' -curves also changes (*Figure 3.13a*).

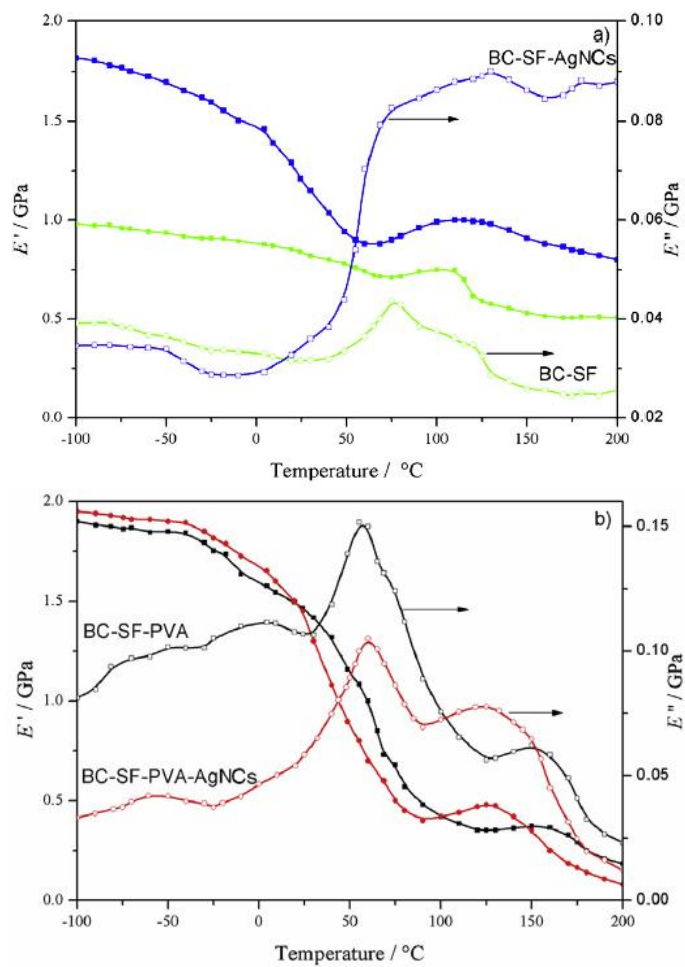


Figure 3.13 Storage (full symbols) and loss (open symbols) shear moduli of the films as a function of temperature. a) BC-SF (S8) and BC-SF-AgNC (S9) samples, b) BC-SF-PVA-AgNC (S7) and BC-SF-PVA (S10) samples. The measurements were carried out under white light illumination

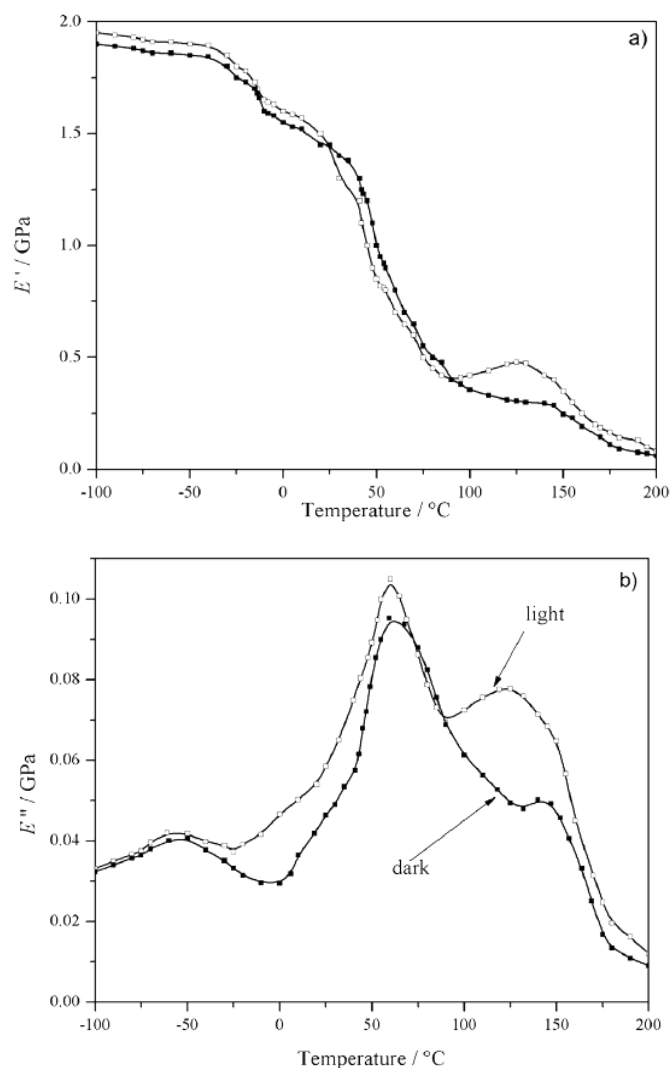


Figure 3.14 a) Storage and b) loss shear moduli of the BC-SF-PVA-AgNC (S7) film recorded in dark (full symbols) and under the white light illumination (open symbols). The frequency of the external force was 1 Hz

This is probably a consequence of the reduced chain mobility of the SF chains induced by nanocubes and also confirmed by DSC results as mentioned earlier. Our result is another provement to the fact that nanostructured silver particles interact well with the polyhydroxylated synthetic- and bio-macromolecules (Raveendran, Fu, & Wallen, 2003 and Mbhele et al., 2003). Recently, we found that the modification of cellulose fibres with spherical silver nanoparticles enhances the mechanical and dynamic mechanical properties of cellulose paper sheets due to improved inter-fibre bonding (Csóka et al., 2012). The losses obviously start to rise dramatically above ~ 25 °C, and the E'' value of the S9 sample at ~ 75 °C is almost two times higher than that of the unmodified BC-SF sample (Figure 3.13a). The T_g of S8 and S9 films are

around 75 °C with an additional transition that appears at ~125 °C. The pure SF films exhibited the transition at higher temperature according to the DMA analysis (Tsukada, Freddi, Kasai, & Monti, 1998), which implies that the E'' peaks noticed in the spectra of both samples at higher temperatures originates from SF (*Figure 3.13a*). The solvent used in the preparation of SF film (water or methanol) has an influence on this peak location (temperature) and it is also apparently sensitive to the presence of BC fibres and AgNC. It should also be ascribed that the E'' spectrum of S9 sample displays the presence of an additional peak at low temperature (-50 °C). This is referred to the amplification of some local conformation rearrangements of silver nanocubes; probably they affect the motions of the amorphous parts in cellulose fibres, which exhibit a broad relaxation transition in that temperature range (Roylance, McElroy, & McGarry, 1980). The relaxation transition at - 50 °C is also more pronounced in the S7 film, attributed to the motion of the amorphous cellulose chains (*Figure 3.13b*). The dependence of the storage shear moduli of S10 and S7 films on temperature is similar to that of the pure PVA polymer from -50 °C until the T_g of PVA (~75 °C) (Khoonsap et al., 2017 and Zhou et al., 2012). With respect to the glass transition peak of the S10 sample, the glass transition of S7 sample is slightly shifted to higher temperature due to reduced mobility of PVA chains in the presence of silver nanocubes (E''-spectra in *Figure 3.13b*). On the other hand, another relaxation process displays at higher temperature above the glass transition, storage curves of both samples show additional fall, which is not present in the curves of pure PVA (Khoonsap et al., 2017 and Zhou et al., 2012). This indeed was observed in the loss moduli spectra of S7 and S10 samples (*Figure 3.13b*) and, according to the results presented in *Figure 3.13a*, the additional process is probably related to SF. In the case of S7 sample, this process has higher intensity and takes place at much lower temperature (~125 °C) than the same process in the spectrum of S10 (~170 °C). The observed shift of the position of the relaxation peak towards lower temperature in the presence of nanostructured silver particles might be the result of the altered interaction of BC and SF. The silver nanocubes obviously affect the motion of all three components in the film (BC, SF and/or PVA). It will further present that the viscoelastic properties of the S7 film at elevated temperature are very sensitive to the presence of light during the DMA experiment. The storage (E') and loss (E'') shear moduli curves of S7 film recorded in the dark and under illumination with white light

are showed in *Figure 3.14*. As can be seen, changing the conditions of the measurements induce changes in storage moduli behaviour in the range from 90 to 150 °C (*Figure 3.14a*). The illuminated sample even undergoes hardening (E' is increasing in the range from 90 to 125 °C) implying the photons somehow cause the rearrangement of the constituents of the film. This is followed by increased losses in the material i.e. the highest temperature E'' -peak of the illuminated sample present much higher intensity than that of the same sample recorded in the dark (*Figure 3.14b*). Also, this peak is positioned at lower temperature (~ 125 °C) when the light is on than when the light is off (~ 140 °C). Dependence of the viscoelastic properties at elevated temperature on the illumination of the S7 sample is an interesting result and is strongly related to the presence of silver nanocubes (as can be seen in *Figure 3.14b*, S10 sample recorded under the illumination shows low intensity transition at ~ 170 °C). It should be mentioned that dielectric cubes could assemble under the influence of light (Petchsang, McDonald, Sinks, & Kuno, 2013). The photo-illumination can produce large number of charge carriers, and consequently an increase in dipole moments, which might cause the alignment. In this case, the illumination probably induces similar effects in BC fibres i.e. a rise in dipole moments, which are obviously amplified in the presence of silver nanocubes. These effects might not be significant below the glass transition temperature. However, above the glass transition, the mobility of the matrix chains is much higher and the photo-illumination effects may contribute to the shear forces induced by external periodic loading. For this reason, there is a strong influence of light on the position and intensity of the high-temperature relaxation transition in S7 sample. Finally, it should be emphasized that the temperature of the sample did not increase significantly during the illumination (~ 0.1 °C) and it is believed that the observed effects are more the result of the formation of photo induced charge carriers than the result of the heating of the sample.

According to *Figure 3.15*, the shear storage modulus and tan delta results for tests carried out showed at different frequencies (0.2 to 20 Hz) at room temperature for basic BC and BC-SF samples.

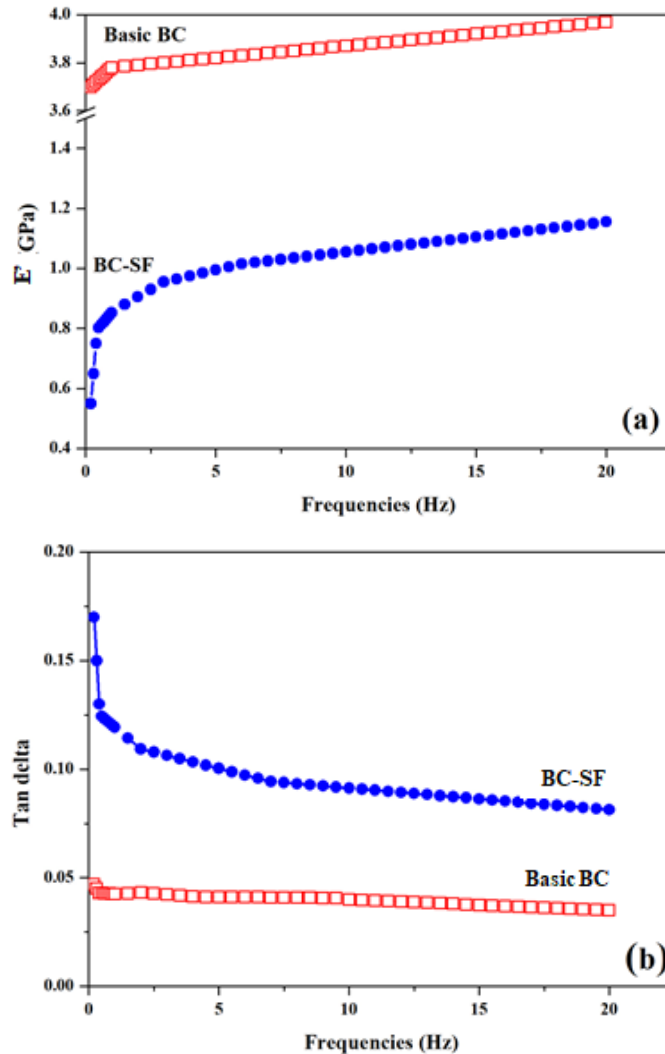


Figure 3.15 Storage modulus (E') and dynamic loss tangent ($\tan \delta$) at different frequencies (a and b) of basic BC and BC-SF films

It was found that the shear storage modulus (E') values increased with increasing frequency, for both samples. Overall, BC shows excellent elasticity which is due to the crystalline polymer chains in its structure. $\tan \delta$ is the ratio of loss modulus (E'') to the storage modulus (E'). It can be used to explain the movement of the polymer chain molecules and changes in the structure (Yuan, Yao, Huang, Chen, & Shao, 2010). As can be seen from the results, all of the $\tan \delta$ curves decrease significantly down to frequencies of ~ 1 Hz and then remain flat as the frequency continues to increase. At this point, all the samples behaved as elastic films. As can be seen from the curves, it can be concluded that pure BC film had the lowest values of $\tan \delta$, which means that this sample has a better elastic response to applied loads in comparison to the BC-SF samples.

3.10 Complex conductivity (Conductance)

To study the conductivity properties of the substrate, silver nanocubes were incorporated into the films. The electrical conductivity of the samples was measured as shown in *Figure 3.16*. This figure shows the values of specific conductance and specific susceptance of BC-SF-PVA-AgNC (S7), BC-SF (S8), BC-SF-AgNC (S9), and BC-SF-PVA (S10) films at 22 kHz as a function of time. At the beginning of the experiment, the sample was kept in the dark and the white light was applied in the time interval of 47-67 s.

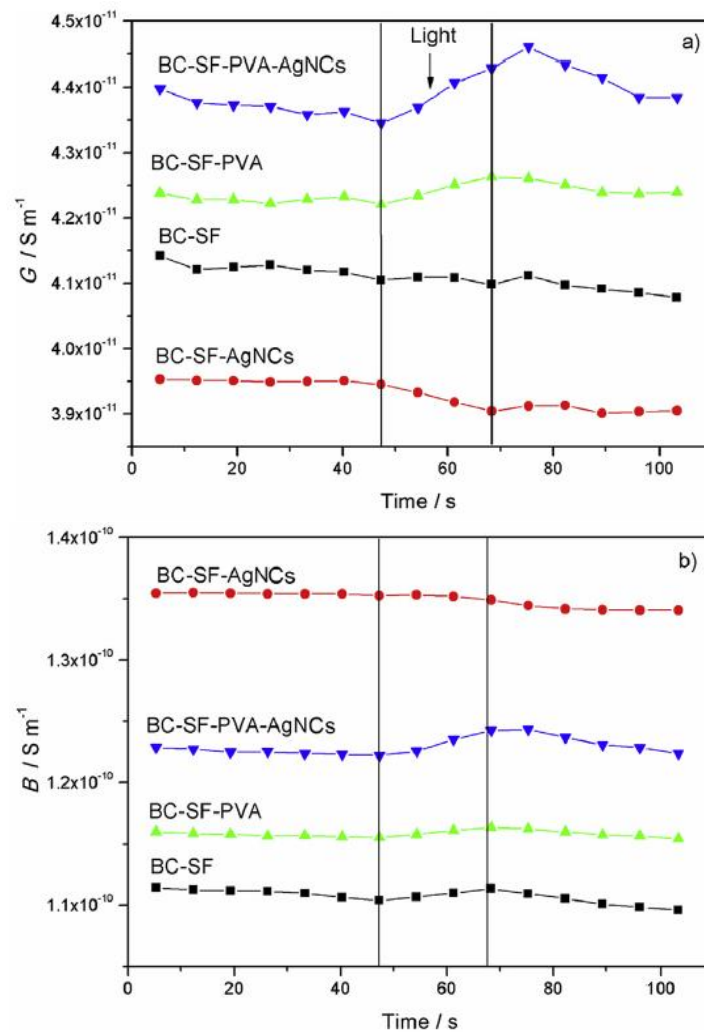


Figure 3.16 Specific a) conductance (G) and b) susceptance (B) of BC-SF-PVA-AgNC (S7), BC-SF (S8), BC-SF-AgNC (S9), and BC-SF-PVA (S10) films at 22 kHz as a function of time. The samples were illuminated in the period of 47-67 s, which is indicated by vertical lines

It can be seen that PVA containing films (S7-S10) are more sensitive to illumination, ie: the specific conductance of these samples increases with application

of light (*Figure 3.16*). This is more pronounced if silver nanocubes are present (S7). The conductance of S8, S9 films is less sensitive to photo-induced effects. As *Figure 3.16* shows, G values of S8, S9 samples slightly decrease with time of the measurement. Obviously, photo-generation of the electrons does not depend solely of the presence of more conductive silver nanocubes. It should be emphasized that the observed changes are small but they directly correspond to the possible effects of light. The measurements were performed in non-contact mode and the photo-induced effects are not shadowed with more pronounced electrode effects. Concerning specific susceptance, the films with AgNCs (S7, S9) show higher losses than nonmodified ones. Except in the case of S9 sample, susceptance slightly increases during the illumination. Relative changes of the specific conductance (ΔG) and susceptance (ΔB) of all samples induced by illumination are presented in *Table 3.6*. They were calculated as the difference between the values obtained at the beginning and at the end of the illumination step (47-67 s).

Table 3.6 Relative changes of specific conductance (ΔG) and susceptance (ΔB) of the films induced by illumination. Sample 7: BC-SF-PVA-AgNC, Sample 8: BC-SF, Sample 9: BC-SF-AgNC, Sample 10: BC-SF-PVA

Sample Number	S7		S8		S9		S10	
	$\Delta G7$	$\Delta B7$	$\Delta G8$	$\Delta B8$	$\Delta G9$	$\Delta B9$	$\Delta G10$	$\Delta B10$
7	0.1	0.85	0.1	-0.3	1.5	1	1.1	2
22	0.02	1.04	-0.37	-0.32	0.96	0.78	2.1	1.7
70	0.25	1.3	-0.42	0.1	1	1.6	1.9	1.4
200	0.57	0.7	-0.15	0.25	1.1	1.1	1.8	1.2

In case of the present substrates, the mentioned main purpose is for producing electronic display especially for mobile phone, which is the electronic device that people use nowadays only for 2-3 years and they will change according to the new trend. Considering to the overall results, it can be concluded that the most favorable films for producing flexible electronic substrate are BC-PVA-AgNC (S4) and BC-SF-PVA-AgNC (S7). Therefore, these kinds of material are prevailing because of its biodegradability, light in weight and flexibility. This work was successful to produce and can be a very good candidate for replacing glass and plastic substrate for the future.

CHAPTER IV

CONCLUSIONS

The main conclusions of the research work can be summarized as follows:

1. The effect of acid hydrolysis and ultrasonication technique were appropriate methods for reducing the size of BC and SF fibrils. Fabrication of flexible, transparent, and self-standing substrate for OLED display was successful by using BC, SF, and PVA as raw materials together with silver nanocubes via normal casting evaporation drying technique as proved by the optical images. Moreover, the silver nanocubes did not affect their intrinsic optical properties (WH:A1-2, WH:CP1-5).
2. The results from FESEM images demonstrated that the surface of BC-SF-PVA-AgNC dried film shows a 3-D fibrous ultrafine network structure, and many pores were filled with silk fibroin and PVA matrix. PVA could better penetrate to the BC-SF fibrils than SF-PVA blend film. Synthesized silver nanocubes exhibited predominantly nanocube shapes with only some nanospheres. BC-SF-PVA-AgNC film displayed good uniform distribution and no aggregation of AgNC (WH:A1).
3. The structure of silk fibroin was characterized by ADXRD analysis. It was found that the nanosilk in this present work is in amorphous state. When nanosilk was blended with basic BC, crystalline structure was observed by ATR-FTIR spectroscopy.
4. The thermal property of samples, the important characteristics of OLED display was studied by DSC and TGA techniques. All of the samples present thermal stability up to 140 °C before melting and 180 °C before degradation. Interestingly, the glass transition peak of BC-SF-PVA-AgNC sample was unrecognized. This fact suggests a highly crosslink structure of the substances (WH:CP1).
5. Silver nanocubes strongly affect the viscoelastic properties of the BC-SF and BC-SF-PVA films. DMA analyses revealed that the silver modified films exhibit much higher storage moduli than their unmodified counterparts, particularly in the case of BC-SF blend. The loss spectra of BC-SF-PVA and BC-SF-PVA-AgNC films showed

the presence of an additional transition at higher temperatures, attributed to the SF component. That transition level was highly sensitive to illumination during the DMA analysis. It had a higher intensity and appeared at low temperature than the transition recorded when the same sample was kept in the dark (WH:A1, WH:CE).

6. The light dependence of the viscoelastic and electrical properties of bacterial cellulose-silk fibroin (BC-SF) and bacterial cellulose-silk fibroin-polyvinyl alcohol (BC-SF-PVA) films modified with silver nanocubes (AgNC) was studied. It was found that the electrical properties of the PVA containing films are more sensitive to light exposure. The illumination of the samples results in a rise of the specific conductance of these samples and this effect is more pronounced after introduction of the silver nanocubes. On the other hand, the specific conductance of the BC-SF and BC-SF-AgNC films was almost unaffected by illumination (WH:A1, WH:CP1-3).

7. This work was successful to produce flexible and transparent OLED display that can be a very good candidate for replacing glass and plastic substrate in the future. The most outstanding samples for producing flexible electronic substrate are BC-PVA-AgNC (S4) and BC-SF-PVA-AgNC (S7) as proved by the overall results. These kinds of natural materials are prevailing because of its biodegradability, high thermal stability, mechanical strength, and electrical conductivity.

ACKNOWLEDGEMENTS

Firstly, I would like to acknowledge the Human Resource Development Programme (HRDOP 3.6.1-16-2016-00018) “Improving the role of research + development + innovation in the higher education through institutional developments assisting intelligent specialization in Sopron and Szombathely” at University of West Hungary. This research was fulfilled in the Institute of Wood Based Products and Technologies, Simonyi Károly Faculty of Engineering, Wood Sciences and Applied Arts at University of Sopron during 2016-2019. The work was accomplished as partial fulfillment of the requirements for the degree of doctor of philosophy.

I would like to express my sincere gratitude to my supervisor Prof. Dr. Levente Csóka who gave me the opportunity to study Ph.D. and supported to do this research. He is full of patience, motivation, and immense knowledge. I consider it as a great opportunity to do my doctoral programme under his advice and to learn from his research expertise. Without his precious support, it would not be possible to conduct this work.

Besides my supervisor, my sincere thanks also go to Thongaumphai’s family for their providing raw Nata de coco during the experiment. I would like to acknowledge Dr. Duško Dudić and Dr. Vladimir Djoković, Vinča Institute of Nuclear Sciences, University of Belgrade, Serbia for their meticulous support in electrical measurements. I appreciate them for all their helps and efforts. I would like to thank Ms. Charu Agarwal, Ph.D. student at University of Sopron, for XRD measurements on ADXRD beamline (BL12) using Indus-2 synchrotron source, RRCAT (India). I would also like to thank the expert who was involved in the DSC and TGA laboratories at METTLER-TOLEDO (Thailand) limited, Ms.Pattra Janthanasakulwong for the professional guidance during I carried out the research work.

No research is possible without Dr. Katalin Halász, Dr. Ádám Makk, and Dr. Éva Papp and other staff who have been very helpful and was always kind to me.

Last but not least, I must express my very profound gratitude to my beloved parents; Narin-Wanna Hosakun, my dear sister; Dr. Yanin Hosakun, and friends, especially,

Tóth Annamária, for their inspiration, continuous encouragement, understanding, love, and support in every possible way to see the completion of this research. This achievement would not have been possible without them. Thank you.

List of My Publications

WH:A1:Worakan Hosakun, Yanin Hosakun, Duško Dudić, Vladimir Djoković, and Levente Csóka. “Dependence of mechanical and electrical properties of silver nanocubes impregnated bacterial cellulose-silk fibroin-polyvinyl alcohol films on light exposure” *Polymer Testing Journal*, vol. 71, 110-114, 2018.

WH:A2: Worakan Hosakun, Levente Csóka. “Study of bacterial cellulose composite films by dynamic mechanical analysis” (submitted).

WH:CP1: Worakan Hosakun, Yanin Hosakun, Duško Dudić, Vladimir Djoković, and Levente Csóka. “Thermal and electrical properties of transparent and flexible films based on bacterial cellulose-silk fibroin-polyvinyl alcohol impregnated with silver nanocubes for flexible electronic display” 6th International Scientific Conference on Advances in Mechanical Engineering (ISCAME). Meeting place and date: Faculty of Engineering, University of Debrecen, Hungary, 2018.10.11-2018.10.12.

WH:CE: Worakan Hosakun. “Study of bacterial cellulose composite films by dynamic mechanical analysis” PhD Complex Exam Presentation at University of Sopron, 2018.

WH:CP2: Worakan Hosakun, Levente Csóka. “Properties of bacterial cellulose nanocomposite films with and without silver nanowires for electronic display” 7th Interdisciplinary Doctoral Conference 2018. Meeting place and date: University of Pécs, Hungary, 2018.05.17-2018.05.19.

WH:CP3: Worakan Hosakun, Levente Csóka. “Study of bacterial cellulose composite films with and without silver nanowires by dynamic mechanical analysis” 5th EPNOE International Polysaccharide Conference 2017. Meeting

place and date: University of Applied Sciences Jena, Germany, 2017.08.20-2018.08.24.

WH:CP4: Worakan Hosakun, Levente Csóka. “Study of bacterial cellulose nanocomposite films by dynamic mechanical analysis” COST Action FP1205: Innovative Applications of Cellulose Fibers Regenerate Wood: Cellulosic material properties and industrial potential - Final meeting in COST FP1205. Meeting place and date: KTH Royal Institute of Technology, Stockholm, Sweden, 2017.03.07-2017.03.09.

WH:CP5: Worakan Hosakun, Levente Csóka. “Fabrication of bacterial cellulose and bacterial cellulose/silk fibroin embedded in silver nanowires for flexible electronic displays” PhD Conference at University of Sopron, 2017.

CHAPTER V

REFERENCES

1. Acharya, C., Ghosh, S. K., & Kundu, S. C. (2008). Silk fibroin protein from mulberry and non-mulberry silkworms: cytotoxicity, biocompatibility and kinetics of L929 murine fibroblast adhesion. *Journal of Materials Science: Materials in Medicine*, 19(8), 2827-2836. doi:10.1007/s10856-008-3408-3
2. Bacterial cellulose. Retrieved from https://application.wiley-vch.de/books/biopoly/pdf_v05/bpol5003_37_46.pdf/
3. Baker, M. I., Walsh, S. P., Schwartz, Z., & Boyan, B. D. (2012). A review of polyvinyl alcohol and its uses in cartilage and orthopedic applications. *Journal of Biomedical Materials Research Part B: Applied Biomaterials*, 100B(5), 1451-1457. doi:doi:10.1002/jbm.b.32694
4. Battista, O. A. (1950). Hydrolysis and Crystallization of Cellulose. *Industrial & Engineering Chemistry*, 42(3), 502-507. doi:10.1021/ie50483a029
5. Berkhout, A. MSc. Thesis. Silver nanocubes as building blocks for a transparent conductive network. Faculty of Physics, Track Advanced Matter and Energy Physics, Universiteit Van Amsterdam. 2015.
6. Bondeson, D., & Oksman, K. (2007). Polylactic acid/cellulose whisker nanocomposites modified by polyvinyl alcohol. *Composites Part A: Applied Science and Manufacturing*, 38(12), 2486-2492. doi:<https://doi.org/10.1016/j.compositesa.2007.08.001>

7. Chawla, P., Bajaj, I., Survase, S., & S. Singhal, R. (2009). Microbial Cellulose: Fermentative Production and Applications (Vol. 47).
8. Chen, C.-W., Hsieh, P.-Y., Chiang, H.-H., Lin, C.-L., Wu, H.-M., & Wu, C.-C. (2003). Top-emitting organic light-emitting devices using surface-modified Ag anode. *Applied Physics Letters*, 83(25), 5127-5129. doi:10.1063/1.1635076
9. Csóka, L., Božanić, D. K., Nagy, V., Dimitrijević-Branković, S., Luyt, A. S., Grozdits, G., & Djoković, V. (2012). Viscoelastic properties and antimicrobial activity of cellulose fiber sheets impregnated with Ag nanoparticles. *Carbohydrate Polymers*, 90(2), 1139-1146. doi:<https://doi.org/10.1016/j.carbpol.2012.06.065>
10. Daniel, L., Gaël, G., Céline, M., Caroline, C., Daniel, B., & Jean-Pierre, S. (2013). Flexible transparent conductive materials based on silver nanowire networks: a review. *Nanotechnology*, 24(45), 452001.
11. Flexible Electronics: Materials and Applications. (2009) Retrieved from https://books.google.hu/books?hl=en&lr=&id=ZiGjrlkSpOQC&oi=fnd&pg=PR1&dq=flexible+electronics+:+materials+and+applications&ots=cKNMQoqPYs&sig=yv1hidsVm210tbJVqnRtPjYFVpl&redir_esc=y#v=onepage&q=flexible%20electronics%20%3A%20materials%20and%20applications&f=false/
12. Foresti, M. L., Vázquez, A., & Boury, B. (2017). Applications of bacterial cellulose as precursor of carbon and composites with metal oxide, metal sulfide and metal nanoparticles: A review of recent advances. *Carbohydrate Polymers*, 157, 447-467. doi:<https://doi.org/10.1016/j.carbpol.2016.09.008>

13. Ha, S.-W., Gracz, H. S., Tonelli, A. E., & Hudson, S. M. (2005). Structural Study of Irregular Amino Acid Sequences in the Heavy Chain of *Bombyx mori* Silk Fibroin. *Biomacromolecules*, 6(5), 2563-2569. doi:10.1021/bm050294m
14. Habibi, Y., Lucia, L., & Rojas, O. (2010). *Cellulose Nanocrystals: Chemistry, Self-Assembly, and Applications* (Vol. 110).
15. Han, T.-H., Lee, Y., Choi, M.-R., Woo, S.-H., Bae, S.-H., Hong, B. H., Lee, T.-W. (2012). Extremely efficient flexible organic light-emitting diodes with modified graphene anode. *Nature Photonics*, 6, 105. doi:10.1038/nphoton.2011.318
<https://www.nature.com/articles/nphoton.2011.318#supplementary-information>
16. Han, X., Chen, S., & Hu, X. (2009). Controlled-release fertilizer encapsulated by starch/polyvinyl alcohol coating. *Desalination*, 240(1), 21-26. doi:<https://doi.org/10.1016/j.desal.2008.01.047>
17. Hofmann, S., Wong Po Foo, C. T., Rossetti, F., Textor, M., Vunjak-Novakovic, G., Kaplan, D. L., Meinel, L. (2006). Silk fibroin as an organic polymer for controlled drug delivery. *Journal of Controlled Release*, 111(1), 219-227. doi:<https://doi.org/10.1016/j.jconrel.2005.12.009>
18. Hosakun, Y. Ph.D. Thesis. ATR-FTIR Study of the Interaction of CO₂ with Bacterial cellulose-Based Membranes. Faculty of Engineering, Wood Sciences and Applied Arts, Univeristy of Sopron. 2017.
19. Hosakun, Y., Halász, K., Horváth, M., Csóka, L., & Djoković, V. (2017). ATR-FTIR study of the interaction of CO₂ with bacterial cellulose-based

- membranes. *Chemical Engineering Journal*, 324, 83-92.
doi:<https://doi.org/10.1016/j.cej.2017.05.029>
20. Hota, M. K., Bera, M. K., Kundu, B., Kundu, S. C., & Maiti, C. K. (2012). A Natural Silk Fibroin Protein-Based Transparent Bio-Memristor. *Advanced Functional Materials*, 22(21), 4493-4499. doi:[doi:10.1002/adfm.201200073](https://doi.org/10.1002/adfm.201200073)
21. Hu, L., Kim, H. S., Lee, J.-Y., Peumans, P., & Cui, Y. (2010). Scalable Coating and Properties of Transparent, Flexible, Silver Nanowire Electrodes. *ACS Nano*, 4(5), 2955-2963. doi:[10.1021/nn1005232](https://doi.org/10.1021/nn1005232)
22. IFA 2015 Directions for LG Electronics' OLED TV?. (2015, September) Retrieved from <http://en.olednet.com/ifa-2015-directions-for-lg-electronics-oled-tv/>
23. Jiang, P., Liu, H., Wang, C., Wu, L., Huang, J., & Guo, C. (2006). Tensile behavior and morphology of differently degummed silkworm (*Bombyx mori*) cocoon silk fibres. *Materials Letters*, 60(7), 919-925.
doi:<https://doi.org/10.1016/j.matlet.2005.10.056>
24. Juby, K. A., Dwivedi, C., Kumar, M., Kota, S., Misra, H. S., & Bajaj, P. N. (2012). Silver nanoparticle-loaded PVA/gum acacia hydrogel: Synthesis, characterization and antibacterial study. *Carbohydrate Polymers*, 89(3), 906-913. doi:<https://doi.org/10.1016/j.carbpol.2012.04.033>
25. Jung, R., Kim, H.-S., Kim, Y., Kwon, S.-M., Lee, H. S., & Jin, H.-J. (2008). Electrically conductive transparent papers using multiwalled carbon nanotubes.

- Journal of Polymer Science Part B: Polymer Physics, 46(12), 1235-1242.
doi:doi:10.1002/polb.21457
26. Karzazi, Y. (2014). *Organic light emitting diodes: Devices and applications* (Vol. 5).
 27. Kawai, F., & Hu, X. (2009). Biochemistry of microbial polyvinyl alcohol degradation. *Applied Microbiology and Biotechnology*, 84(2), 227. doi:10.1007/s00253-009-2113-6
 28. Khoonsap, S., Rugmai, S., Hung, W.-S., Lee, K.-R., Klinrisuk, S., & Amnuaypanich, S. (2017). Promoting permeability-selectivity anti-trade-off behavior in polyvinyl alcohol (PVA) nanocomposite membranes. *Journal of Membrane Science*, 544, 287-296. doi:<https://doi.org/10.1016/j.memsci.2017.09.035>
 29. Kljun, A., Benians, T. A. S., Goubet, F., Meulewaeter, F., Knox, J. P., & Blackburn, R. S. (2011). Comparative Analysis of Crystallinity Changes in Cellulose I Polymers Using ATR-FTIR, X-ray Diffraction, and Carbohydrate-Binding Module Probes. *Biomacromolecules*, 12(11), 4121-4126. doi:10.1021/bm201176m
 30. Koh, L.-D., Cheng, Y., Teng, C.-P., Khin, Y.-W., Loh, X.-J., Tee, S.-Y., Han, M.-Y. (2015). Structures, mechanical properties and applications of silk fibroin materials. *Progress in Polymer Science*, 46, 86-110. doi:<http://dx.doi.org/10.1016/j.progpolymsci.2015.02.001>

31. Kundu, S. C., Dash, B. C., Dash, R., & Kaplan, D. L. (2008). Natural protective glue protein, sericin bioengineered by silkworms: Potential for biomedical and biotechnological applications. *Progress in Polymer Science*, 33(10), 998-1012. doi:<https://doi.org/10.1016/j.progpolymsci.2008.08.002>
32. Kunić, S., & Šego, Z. (2012, 12-14 Sept. 2012). OLED technology and displays. Paper presented at the Proceedings ELMAR-2012.
33. Lee, J. H., Song, D. W., Park, Y. H., & Um, I. C. (2016). Effect of residual sericin on the structural characteristics and properties of regenerated silk films. *International Journal of Biological Macromolecules*, 89, 273-278. doi:<https://doi.org/10.1016/j.ijbiomac.2016.04.073>
34. Lee, K.-Y., Buldum, G., Mantalaris, A., & Bismarck, A. (2014). More Than Meets the Eye in Bacterial Cellulose: Biosynthesis, Bioprocessing, and Applications in Advanced Fiber Composites. *Macromolecular Bioscience*, 14(1), 10-32. doi:[doi:10.1002/mabi.201300298](https://doi.org/10.1002/mabi.201300298)
35. Legnani, C., Vilani, C., Calil, V. L., Barud, H. S., Quirino, W. G., Achete, C. A., Cremona, M. (2008). Bacterial cellulose membrane as flexible substrate for organic light emitting devices. *Thin Solid Films*, 517(3), 1016-1020. doi:<https://doi.org/10.1016/j.tsf.2008.06.011>
36. Li, W., Yue, J., & Liu, S. (2012). Preparation of nanocrystalline cellulose via ultrasound and its reinforcement capability for poly(vinyl alcohol) composites. *Ultrasonics Sonochemistry*, 19(3), 479-485. doi:<https://doi.org/10.1016/j.ultsonch.2011.11.007>

37. Li, Y. Thesis. Studies on the cellulose hydrolysis and hemicellulose monosaccharide degradation in concentrated hydrochloric acid. Faculty of Graduate and Postdoctoral Studies in partial fulfillment of the requirements for the degree of Master of Applied Science, University of Ottawa. 2014.
38. Lighting. (2013, May) Retrieved from <https://studylib.net/doc/18747308/lighting>.
39. Linder, T. Ph.D. Thesis. Light scattering in fiber-based materials - A foundation for characterization of structural properties. Department of Computer Science, Electrical and Space Engineering, Luleå University of Technology, 2014.
40. Ling, S., Qi, Z., Knight, D. P., Shao, Z., & Chen, X. (2013). FTIR imaging, a useful method for studying the compatibility of silk fibroin-based polymer blends. *Polymer Chemistry*, 4(21), 5401-5406. doi:10.1039/C3PY00508A
41. Liu, Y., Qi, N., Song, T., Jia, M., Xia, Z., Yuan, Z., Sun, B. (2014). Highly Flexible and Lightweight Organic Solar Cells on Biocompatible Silk Fibroin. *ACS Applied Materials & Interfaces*, 6(23), 20670-20675. doi:10.1021/am504163r
42. Lu, J., Wang, T., & Drzal, L. T. (2008). Preparation and properties of microfibrillated cellulose polyvinyl alcohol composite materials. *Composites Part A: Applied Science and Manufacturing*, 39(5), 738-746. doi:<https://doi.org/10.1016/j.compositesa.2008.02.003>

43. Luo, Q., Chen, Z., Hao, X., Zhu, Q., & Zhou, Y. (2013). Preparation and properties of nanometer silk fibroin peptide/polyvinyl alcohol blend films for cell growth. *International Journal of Biological Macromolecules*, 61, 135-141. doi:<https://doi.org/10.1016/j.ijbiomac.2013.06.050>
44. Mbhele, Z. H., Salemane, M. G., van Sittert, C. G. C. E., Nedeljković, J. M., Djoković, V., & Luyt, A. S. (2003). Fabrication and Characterization of Silver–Polyvinyl Alcohol Nanocomposites. *Chemistry of Materials*, 15(26), 5019-5024. doi:10.1021/cm034505a
45. Melke, J., Midha, S., Ghosh, S., Ito, K., & Hofmann, S. (2016). Silk fibroin as biomaterial for bone tissue engineering. *Acta Biomaterialia*, 31, 1-16. doi:<https://doi.org/10.1016/j.actbio.2015.09.005>
46. Mohd Amin, M. C. I., Abadi, A., Ahmad, N., Katas, H., & Jamal, J. (2012). Bacterial Cellulose Film Coating as Drug Delivery System: Physicochemical, Thermal and Drug Release Properties (Vol. 41).
47. Nogi, M., & Yano, H. (2008). Transparent Nanocomposites Based on Cellulose Produced by Bacteria Offer Potential Innovation in the Electronics Device Industry. *Advanced Materials*, 20(10), 1849-1852. doi:[doi:10.1002/adma.200702559](https://doi.org/10.1002/adma.200702559)
48. Okahisa, Y., Yoshida, A., Miyaguchi, S., & Yano, H. (2009). Optically transparent wood–cellulose nanocomposite as a base substrate for flexible organic light-emitting diode displays. *Composites Science and Technology*, 69(11), 1958-1961. doi:<https://doi.org/10.1016/j.compscitech.2009.04.017>

49. Oliveira Barud, H. G., Barud, H. d. S., Cavicchioli, M., do Amaral, T. S., Junior, O. B. d. O., Santos, D. M., Ribeiro, S. J. L. (2015). Preparation and characterization of a bacterial cellulose/silk fibroin sponge scaffold for tissue regeneration. *Carbohydrate Polymers*, 128, 41-51. doi:<https://doi.org/10.1016/j.carbpol.2015.04.007>
50. Ougiya, H., Watanabe, K., Matsumura, T., & Yoshinaga, F. (1998). Relationship between Suspension Properties and Fibril Structure of Disintegrated Bacterial Cellulose. *Bioscience, Biotechnology, and Biochemistry*, 62(9), 1714-1719. doi:10.1271/bbb.62.1714
51. Petchsang, N., McDonald, M. P., Sinks, L. E., & Kuno, M. (2013). Light Induced Nanowire Assembly: The Electrostatic Alignment of Semiconductor Nanowires into Functional Macroscopic Yarns. *Advanced Materials*, 25(4), 601-605. doi:doi:10.1002/adma.201202722
52. Rankel, S. (2004). OLEDs - Organic Light Emitting Diodes. Seminar: University of Ljubljana, Faculty of Mathematic and Physics, Department of Physics. Retrieved from http://mafija.fmf.uni-lj.si/seminar/files/2003_2004/OLEDs.pdf/
53. Raveendran, P., Fu, J., & Wallen, S. L. (2003). Completely "Green" Synthesis and Stabilization of Metal Nanoparticles. *Journal of the American Chemical Society*, 125(46), 13940-13941. doi:10.1021/ja029267j
54. Roohani, M., Habibi, Y., Belgacem, N. M., Ebrahim, G., Karimi, A. N., & Dufresne, A. (2008). Cellulose whiskers reinforced polyvinyl alcohol copolymers nanocomposites. *European Polymer Journal*, 44(8), 2489-2498. doi:<https://doi.org/10.1016/j.eurpolymj.2008.05.024>

55. Roylance, D., McElroy, P., & McGarry, F. (1980). Viscoelastic properties of paper. *Fibre Science and Technology*, 13(6), 411-421.
56. Santos, S. M., Carbajo, J. M., Quintana, E., Ibarra, D., Gomez, N., Ladero, M., Villar, J. C. (2015). Characterization of purified bacterial cellulose focused on its use on paper restoration. *Carbohydrate Polymers*, 116, 173-181. doi:<https://doi.org/10.1016/j.carbpol.2014.03.064>
57. Shang, S., Zhu, L., & Fan, J. (2013). Intermolecular interactions between natural polysaccharides and silk fibroin protein. *Carbohydrate Polymers*, 93(2), 561-573. doi:<http://dx.doi.org/10.1016/j.carbpol.2012.12.038>
58. Silk. (2016, June) Retrieved from <https://oecotextiles.wordpress.com/tag/bombyx-mori/>
59. Size Scale of Cellulose-based Particles. Retrieved from <https://engineering.purdue.edu/nanotrees/>
60. Sulaeva, I., Henniges, U., Rosenau, T., & Potthast, A. (2015). Bacterial cellulose as a material for wound treatment: Properties and modifications. A review. *Biotechnology Advances*, 33(8), 1547-1571. doi:<http://dx.doi.org/10.1016/j.biotechadv.2015.07.009>
61. Teramoto, H., & Kojima, K. (2014). Production of Bombyx mori Silk Fibroin Incorporated with Unnatural Amino Acids. *Biomacromolecules*, 15(7), 2682-2690. doi:10.1021/bm5005349

62. The Glass Transition. (2018) Retrieved from <https://pslc.ws/macrog/tg.htm/>
63. Tsalagkas, D. Ph.D. Thesis. Bacterial cellulose thin-films for energy harvesting applications. Faculty of Engineering, Wood Sciences and Applied Arts, Univeristy of West Hungary. 2015.
64. Tsukada, M., Freddi, G., Kasai, N., & Monti, P. (1998). Structure and molecular conformation of tussah silk fibroin films treated with water–methanol solutions: Dynamic mechanical and thermomechanical behavior. *Journal of Polymer Science Part B: Polymer Physics*, 36(15), 2717-2724.
65. Um, I. C., Kweon, H., Park, Y. H., & Hudson, S. (2001). Structural characteristics and properties of the regenerated silk fibroin prepared from formic acid. *International Journal of Biological Macromolecules*, 29(2), 91-97. doi:[https://doi.org/10.1016/S0141-8130\(01\)00159-3](https://doi.org/10.1016/S0141-8130(01)00159-3)
66. Ummartyotin, S., Juntaro, J., Sain, M., & Manuspiya, H. (2012). Development of transparent bacterial cellulose nanocomposite film as substrate for flexible organic light emitting diode (OLED) display. *Industrial Crops and Products*, 35(1), 92-97. doi:<http://dx.doi.org/10.1016/j.indcrop.2011.06.025>
67. Unit - Chemistry of Garments: Animal Fibres. (2016) Retrieved from http://wwwchem.uwimona.edu.jm/courses/CHEM2402/Textiles/Animal_Fibres.html/
68. What is OLED and how does it work. (2016) Retrieved from <https://www.scienceabc.com/innovation/what-is-oled-and-how-does-it-work.html/>

69. What makes it the best TV ever. Retrieved from <https://www.lg.com/us/experience-tvs/oled-tv/oled-vs-led/>
70. Wu, X., Liu, X.-Y., Du, N., Xu, G., & Li, B. (2009). Unraveled mechanism in silk engineering: Fast reeling induced silk toughening. *Applied Physics Letters*, 95(9), 093703. doi:10.1063/1.3216804
71. Yang, G., Zhang, L., & Liu, Y. (2000). Structure and microporous formation of cellulose/silk fibroin blend membranes: I. Effect of coagulants. *Journal of Membrane Science*, 177(1), 153-161. doi:[https://doi.org/10.1016/S0376-7388\(00\)00467-1](https://doi.org/10.1016/S0376-7388(00)00467-1)
72. Yang, H., Xu, S., Jiang, L., & Dan, Y. (2012). Thermal Decomposition Behavior of Poly (Vinyl Alcohol) with Different Hydroxyl Content. *Journal of Macromolecular Science, Part B*, 51(3), 464-480. doi:10.1080/00222348.2011.597687
73. Yano, H., Sugiyama, J., Nakagaito, A. N., Nogi, M., Matsuura, T., Hikita, M., & Handa, K. (2005). Optically Transparent Composites Reinforced with Networks of Bacterial Nanofibers. *Advanced Materials*, 17(2), 153-155. doi:10.1002/adma.200400597
74. Yuan, Q., Yao, J., Huang, L., Chen, X., & Shao, Z. (2010). Correlation between structural and dynamic mechanical transitions of regenerated silk fibroin. *Polymer*, 51(26), 6278-6283. doi:<http://dx.doi.org/10.1016/j.polymer.2010.10.046>

75. Zhou, K., Jiang, S., Bao, C., Song, L., Wang, B., Tang, G., . . . Gui, Z. (2012). Preparation of poly(vinyl alcohol) nanocomposites with molybdenum disulfide (MoS₂): structural characteristics and markedly enhanced properties. *RSC Advances*, 2(31), 11695-11703. doi:10.1039/C2RA21719H

Appendix

The spacing between the planes calculation

According to the equation below, the spacing between the planes of each sample were calculated;

$$\lambda = 2d\sin\theta,$$

where, the wavelength (λ) is 1.1 Å, d is the spacing between the planes, and θ is the half the angle 2θ .

Specific conductivity

In order to calculate the specific conductivity of the samples, we assumed that the electric field do not change significantly when the sample is in the cell and when the sample is empty i.e. we used the effective voltage on the electrodes in both cases. Considering that the films are very thin, (~ 30 μm for BC-SF and ~ 80 μm BC-SF-PVA) this assumption seemed reasonable. On the other hand, this procedure enabled us to measure direct effects of the illumination on the complex conductivity samples and to avoid the pronounced electrode effects. In the present approach, we first determined the specific conductivity (σ_s) after introduction of the sample into the cell as

$$\sigma_s = \frac{U_{eff}}{I},$$

where, effective voltage on the electrodes and I is the electrical current through the sample. Specific conductivity of the film (σ_o) is then calculated as

$$\sigma_o = \frac{U_{eff}}{ES} \sigma_s,$$

where $E = U_{eff}/d$ is the electric field in the sample and the S is the surface of the sample.